A transformable nanoplatform with multiple therapeutic and immunostimulatory properties for treatment of advanced cancers

Published version:

DOI:10.1016/j.biomaterials.2023.122145

A transformable nanoplatform with multiple therapeutic and immunostimulatory properties for treatment of advanced cancers

Xiangdong Xue[1] , Haijing Qu[1] , Ruonan Bo[2] , Dalin Zhang[3] , Zheng Zhu[4] , Bai Xiang[5] , Longmeng Li[3] , Marina Ricci[3] , Chong-Xian Pan[6] , Tzu-Yin Lin[7] , Yuanpei Li[8]

[1] School of Pharmacy, National Key Laboratory of Innovative Immunotherapy, Shanghai Jiao Tong University, Shanghai, 200240, China; Department of Biochemistry and Molecular Medicine, UC Davis Comprehensive Cancer Center, University of California Davis, Sacramento, CA, 95817, USA.
[2] Department of Biochemistry and Molecular Medicine, UC Davis Comprehensive Cancer Center, University of California Davis, Sacramento, CA, 95817, USA; School of Veterinary Medicine, Yangzhou University, Yangzhou, 225009, China.
[3] Department of Biochemistry and Molecular Medicine, UC Davis Comprehensive Cancer Center, University of California Davis, Sacramento, CA, 95817, USA.
[4] Brigham and Women's Hospital, Harvard Medical School, Boston, MA, 02132, USA.
[5] Department of Biochemistry and Molecular Medicine, UC Davis Comprehensive Cancer Center, University of California Davis, Sacramento, CA, 95817, USA; Key Laboratory of Hebei Province for Innovative Drug Research and Evaluation, School of Pharmaceutical Sciences, Hebei Medical University, Shijiazhuang, Hebei, 050017, China.
[6] Brigham and Women's Hospital, Harvard Medical School, Boston, MA, 02132, USA; VA Boston Healthcare System, Boston, MA, 02132, USA.
[7] Division of Hematology and Oncology, Department of Internal Medicine, School of Medicine, University of California Davis, Sacramento, CA, 95817, USA.
[8] Department of Biochemistry and Molecular Medicine, UC Davis Comprehensive Cancer Center, University of California Davis, Sacramento, CA, 95817, USA. Electronic address: lypli@ucdavis.edu.

Abstract

Cancer is a complex pathological phenomenon that needs to be treated from different aspects. Herein, we developed a size/charge dually transformable nanoplatform (PDR NP) with multiple therapeutic and immunostimulatory properties to effectively treat advanced cancers. The PDR NPs exhibit three different therapeutic modalities (chemotherapy, phototherapy and immunotherapy) that can be used to effectively treat primary and distant tumors, and reduce recurrent tumors; the immunotherapy is simultaneously activated by three major pathways, including toll-like receptor, stimulator of interferon genes and immunogenic cell death, effectively suppresses the tumor development in combination with an immune checkpoint inhibitor. In addition, PDR NPs show size and charge responsive transformability in the tumor microenvironment, which overcomes various biological barriers and efficiently delivers the payloads into tumor cells. Taking these unique characteristics together, PDR NPs effectively ablate primary tumors, activate strong anti-tumor immunity to suppress distant tumors and reduce tumor recurrence in bladder tumor-bearing mice. Our versatile nanoplatform shows great potential for multimodal treatments against metastatic cancers.

Keywords

Drug delivery
Multimodal therapy
Phototherapy
Chemotherapy
Immunotherapy

Abbreviations

Pa	pheophorbide a
DOX	doxorubicin hydrochloride
PhD	pheophorbide a-hydrazide-doxorubicin
PEG-2CHO	di-aldehyde functionalized polyethylene glycol
TAM	Tumor associate macrophage
DC	dendritic cell
ICI	immune checkpoint inhibitor
TIME	tumor immune microenvironment
MDSC	myeloid-derived suppressor cells
Treg	regulatory T cell
TAA	tumor-associate antigen
TLR	Toll-like receptor
STING	stimulator of interferon gene
cGAMP	2′, 3′-cyclic guanosine monophosphate–adenosine monophosphate
APC	antigen-presenting cell
ICD	immunogenic cell death
SDS	sodium dodecyl sulfate
ACQ	aggregation-caused quenching
NIRF	near-infrared fluorescence
ROS	reactive oxygen species
PDT	photodynamic therapy
PTT	photothermal therapy
CLSM	confocal laser scanning microscopy
CRT	calreticulin
ER	endoplasmic reticulum
TNF	tumor necrosis factor
CTL	cytotoxic T lymphocytes

1. Introduction

Cancer is a complex pathological phenomenon that involves multiple biological abnormalities. Conventional treatments, such as surgery, radiotherapy and chemotherapy, are barely satisfactory, mainly when cancer develops to an advanced stage with metastasis. Cancer immunotherapy with immune checkpoint inhibitors (ICIs) [1,2] can reactivate anti-cancer immunity and spot metastasis, showing great promise to treat advanced cancer. Although some cancer patients achieve long-term remission, the response rates of immunotherapy are generally low, usually around 20–30% except in a few highly selected patient populations. Among many mechanisms of resistance, little immune cell infiltration (immune "cold") and immunosuppressive tumor immune microenvironment (TIME) are two major mechanisms of resistance [3,4]. Cancer harbors ample immunosuppressive cells, such as tumor-associated macrophages (TAMs), myeloid-derived suppressor cells (MDSCs) and regulatory T cells (Tregs). Various strategies have been used in the clinic to enhance the efficacy of cancer immunotherapy. Vaccination is one of the powerful strategies to reverse the TIME from "cold" to "hot", which utilizes specific antigens to prime cytotoxic T lymphocytes for tumor elimination and stimulate memory T cells for the prevention of tumor regression [4,5]. Dendritic cells (DCs) are sentinel antigen-presenting cells (APCs), which bridge the innate and adaptive immune response by sampling and presenting tumor-associate antigens (TAAs) to T cells. Immature DCs show less capability for T cell priming and induce immune tolerance by depleting T cells or promoting the regulatory T cells. Hence, promotion of DC maturation is a key to unleash the subsequent immune response stimulator of interferon genes (STING) [6,7] and Toll-like receptor (TLR) [8,9] agonists show great potential to promote DC maturation. STING is known to be a central mediator of innate and adaptive immunity, which induces the expression of type I interferon, cytokines, and T cell recruitment factors that result in the activation of DCs and priming of tumor-specific T cells. The STING agonist, such as 2′, 3′-cyclic guanosine monophosphate–adenosine monophosphate (cGAMP) [10,11], shows a promising therapeutic effect in terms of cancer immunotherapy. Other TLR agonists, such as R837 [12,13] and R848 [14,15], can efficiently promote DC maturation and have been extensively employed for cancer immunotherapy. However, strong systemic toxicity, such as cytokine storm, hinders the broad applications of agonists for immunotherapy.

DC is the crucial player in the circle of the immune response, and convergent DC stimulation is an efficient way to reverse the "cold" TIME and facilitate cancer immunotherapy. Extensive studies found that phototherapy-treated tumor cells experience immunogenic cell death (ICD) to elicit an adaptive immune response [[16], [17], [18]]. ICD can release TAAs to promote DC maturation and subsequently prime the T cells. In addition, phototherapy destroys tumor cells to expose their dsDNA fragments, making it possible to activate the STING pathway [19]. To maximally promote the critical functionalities of DCs, we intend to integrate STING, TLR and ICD stimulations in one single nanomedicine. Previously, we developed a Trojan Horse nanotheranostic with excellent photo-/chemo-therapeutic effects, which could ablate orthotopic oral cancer with a 100% complete cure rate on mice [20,21]. We hypothesize that such strong phototherapeutic capacity can induce strong ICD and activate the STING pathway (Scheme 1). To integrate the TLR pathway, a TLR7 agonist (R837) is encapsulated into the Trojan Horse nanotheranostic to form a versatile nanoplatform (PDR NP) that exhibits multiple therapeutic and immunostimulatory properties. The PDR NP is composed of three active pharmaceutical ingredients, including a photosensitizer (pheophorbide a, Pa), a chemo-drug (doxorubicin, DOX) and an immunoadjuvant (R837), exhibits three cancer-treating abilities (including chemotherapy, phototherapy and immunotherapy). Among these therapeutic agents, Pa directly ablates the tumor tissues; DOX and R837 work together with Pa to act on both primary and distant tumors. Moreover, Pa-mediated phototherapy and R837 orchestrate three immune activation pathways (TLR7, ICD and STING) in a single nanoparticle. The PDR NPs were prepared by encapsulating R837 into the PD NPs as illustrated in Scheme 1a. The hydrophobic R837 was encapsulated in the PhD monomer-based micelle and further aggregated into larger nanoparticle by multi-micelle aggregation [[22], [23], [24]]. Then, dialdehydes functionalized poly(ethylene glycol)2000 (PEG-2CHO) was employed to crosslink the assemblies by forming the Schiff base, and yielded the final PDR NPs. As shown in Scheme 1b, PDR NPs preferentially accumulate in tumor site due to altered vasculature and impaired lymphatic drainage [25,26]. When PDR NPs reach cancer cells, the PDR NPs undergo a size and charge transformation to gain deeper penetration and elevated cell uptake [20,21]. Pa exerts phototherapy to ablate the primary tumor; phototherapy induces tumor cells to release TAAs, which can elicit an immunological response like a vaccine does. The light-ablated tumor cells expose their DNA fragments to feed DCs for the activation of STING pathway. Meanwhile, R837 is released from the cancer cells and ingested by immature DC (iDC) [16,27]. R837 and STING activation can promote iDC becoming mature DC (mDC). mDCs present TAAs to T cells, and further recruit more T cells in lymph nodes. Activated T cells attack tumor cells, and kill the primary tumor with PTT and doxorubicin-led chemotherapy. The activated T cells roam in the blood circulation to spot the metastatic tumor, exert abscopal effect and work synergistically with chemotherapy from PDR NPs to slow down the tumor progress. Activated T cells can also differentiate into memory T cells and prevent tumor relapse.

2. Results and discussions

Preparation and characterization of PDR NPs.

The PDR NPs were composed of three key components, a photosensitizer (Pa), a chemo-drug (DOX) and a TLR7 agonist (R837). As shown in Figs. S1–S4, the building blocks, including PhD monomer and PEG-2CHO, were successfully synthesized. The hydrodynamic size of PDR NPs was 99.9 nm (Fig. 1a) with a polydispersity index (PDI) of 0.256. TEM micrograph showed that the PDR NPs are spherical nanoparticle harboring crowds of small nanoparticles (Fig. 1b), which is consistent with the assembly process in Scheme

1. The PEGylation shields the amine groups from DOX, thus reducing the charge of the PDR NPs. As shown in Fig. 1c, the surface charge of the PDR NPs dramatically decreased from 42.5 mV to 12.5 mV after the PEGylation. We speculated that the PEGs blocked the amine groups partially due to the steric hindrance and reaction rate between amines and aldehydes; thus, the PDR NPs still showed a weakly positive charge. By calculation, the encapsulation efficiency (EE%) and loading capacity (LC%) of R837 is 96.7% and 4.7%, respectively. The critical aggregation concentration (CAC) of PDR NPs was measured as 2.18 μM (Fig. S5), supporting that PDR NPs can keep the nanostructure when diluted. The UV–vis spectra were employed to demonstrate the self-assembly of PDR NPs. As shown in Fig. 1d, free R837 displayed two characteristic peaks ranging from 300 nm to 330 nm. In PDR NPs, obvious characteristic peaks of R837 were presented. In comparison, PD NPs (PDR NPs without R837) didn't show the peak due to the lack of R837. In comparison with free Pa, the PD and PDR NPs showed obvious red-shift at the Q-band of Pa, because the large planar chemical structure of Pa tends to form "π~π" stacking in PD or PDR NPs. Pa has intrinsic near-infrared fluorescence (NIRF) that can be used for optical imaging. Therefore, the fluorescence property of PD and PDR NPs was investigated. The Pa in both PD NPs and PDR NPs suffered from aggregation-caused quenching (ACQ) effect [[28], [29], [30]], while the fluorescence can be recovered by adding a detergent (sodium dodecyl sulfate, SDS) which can destroy nanostructures (Fig. 1e). Interestingly, the fluorescence of PDR NPs quenched more but recovered less, which further supported that the hydrophobic R837 facilitated a tighter aggregation of PhD monomers. When PD and PDR NPs with or without SDS were imaged (Fig. 1f), the fluorescence of PD and PDR NPs were both quenched. In striking contrast, the nanoparticles with SDS showed strong fluorescence, which is highly consistent with their fluorescence spectra. As a photosensitizer, Pa absorbs light energy and produces hyperthermia and reactive oxygen species (ROS) to destroy cancer cells. To evaluate the phototherapeutic effects (PTT and PDT), different concentrations of PDR NPs and PD NPs were irradiated by a 680 nm laser, respectively. The photo-induced hyperthermia was recorded by a thermal camera; the ROS production was indicated by the singlet oxygen sensor green (SOSG). As shown in Fig. 1g, the phototherapeutic effects, including PDT and PTT, were both relevant to concentrations of the photosensitizer. The hyperthermia generated by 50 μM PDR NPs reached 58 °C and ample ROS was produced in a concentration-dependent manner, supporting that PDR NPs would exhibit effective photothermal and photodynamic effects for cancer ablation. The nanoparticle stability was investigated by incubating with 10% fetal bovine serum (Fig. 1h), PDR NPs kept stable and showed no big fluctuation in size for more than two weeks. In PDR NPs, the amphiphilic PhD monomers were composed of Pa and DOX, which are attached by a hydrazone bond. The intracellular pH, such as pH 5.0 in the lysosome, can break down the PhD monomers to release DOX and R837. Hence, the accumulated drug release pattern of PDR NPs was evaluated by acidic pH stimulation. As shown in Fig. 1i, PDR NPs were quite stable in the physiological circumstance. The DOX and R837 were both retained in the nanoparticle and showed imperceptible drug release. Under acidic pH (5.0) conditions, DOX was released faster than R837 because the PhD micellar structure was supposed to be broken down first to free the encapsulated R837. In 48 h, both drugs were released more than 75%. The PDR NPs kept stable in physiological pH and serum, but can responsively release the DOX and R837 by a particular stimulation. Such a controllable drug release ensures that PDR NPs efficiently deliver the drugs to the tumor site and responsively release the drug in tumor cells.

Size and charge dual-transformability of PDR NPs.

Similar to the Trojan Horse nanotheranostic [20], PDR NP would also be able to pass different biological barriers by taking advantage of the unique size and charge dual-transformability. As shown in Fig. 2a and Fig. S6&S7, the size of PDR NPs dramatically decreased from 99 nm to 8 nm when incubating in pH 6.5 for 12 h, demonstrating that PDR NPs experienced a "large-to-small" size transformation in TME. The size transformation endowed the PDR NPs with more profound tissue-penetrating capability. As shown in Fig. 2b, the PDR NPs at pH 6.5 could penetrate further in UPPL cell spheroid. The PEGylation shielded the strong positive charge derived from amine groups on DOX at neutral pH, while the amine groups would be re-exposed when the PEGylation detached in pHe. As shown in Fig. 2c, the surface charge of PDR NPs elevated from 12.5 mV to 37 mV when environmental pH decreased from 7.4 to 6.5. The high surface charge can interact with the negative membrane charge [31] to facilitate cellular uptake. As shown in Fig. 2d, the cell uptake of the PDR NPs in pH 6.5 medium was significantly higher than the cells in neutral pH, which would contribute to more efficient drug delivery. This unique size and charge transformability would substantially improve the anti-tumor efficacy due to the highly effective drug delivery capability of PDR NPs.

Cytotoxicity of PDR NPs mediated by photo- and chemo-therapies.

To evaluate the anti-tumor effect at in vitro level, UPPL bladder cancer cells were incubated with PDR NPs and the control materials, including PD NPs, free photosensitizer (Pa), free chemo-drug (DOX), free TLR agonist (R837), a physical mix of the three components (MIX) in PDR NPs and a commercial DOX nanoformulation (Doxil). As shown in Fig. 2e, Pa showed almost no efficacy if no light irradiation was applied. R837 exhibited an imperceptible cell-killing effect, as no immune response existed with pure cancer cell culture. All the materials that contained chemotherapeutic drugs exhibited solid anti-tumor effects, among which Doxil showed relatively weaker efficacy. The photosensitizer-containing groups were then treated with light, in which Pa exhibited an excellent cell-killing effect, indicating the phototherapy was highly effective. All other groups, such as PDR NPs, PD NPs and the physical mixed groups showed higher cell-killing effect than their non-light treated counterparts. We also investigated the cytotoxicity of PDR NPs on healthy cells by incubating PDR NPs with human umbilical vein endothelial cells (HUVECs). As shown in Fig. S8, the PDR NPs didn't induce apparent toxicity to the normal cells at low concentrations ($\leq 10\ \mu M$); they only killed less than 18% of HUVECs even at a high concentration of 50 μM. The cytotoxicity was mainly contributed by the chemotherapeutic effect of doxorubicin. In comparison, the PDR NPs with laser irradiation killed more HUVECs starting from 1 μM, causing 40% cell death at a high concentration of 50 μM, which can be ascribed to the combination of phototherapy and chemotherapy. The toxicity of PDR NPs on HUVECs was much lower than their efforts on cancer cells (Fig. 2e), indicating that the PDR NPs would be safer in normal cells. The less toxicity of PDR NPs to HUVEC cells may be ascribed to the low metabolism of the normal cells. Although the PDR NPs + L showed toxicity to normal cells, their damage to normal tissue can be minimized by directing the light to the tumor tissue. Furthermore, the nanoparticles preferentially accumulate at the tumor site, which could reduce the effect on normal cells.

Controllable phototherapy of PDR NPs.

Phototherapy is highly controllable, which only affects the area that light directed. Hence, UPPL cells were incubated with PD NPs and PDR NPs; a specific area of the treated cells was exposed under laser for live/dead cell stain (Fig. 2f). In the PBS-treated group, the laser-exposed cells were alive, showing no difference from the normal cells due to the lack of photosensitizer. In PD NPs or PDR NPs treated groups, most cells were dead in the laser-directed area while the cells without laser treatment were still alive. In PD and PDR NPs-treated cells, a clear boundary between live and dead cells could be distinguished, indicating that the phototherapy was highly controllable, which can avoid harming the normal tissue by attenuating the laser.

Subcellular distribution of PDR NPs.

Since Pa and DOX both have intrinsic fluorescence, the subcellular distributions of the free DOX, Pa, MIX, Doxil, PD NPs and PDR NPs, were observed by confocal laser scanning microscopy (CLSM). As shown in Fig. 2g, free DOX mostly distributed in the nucleus; Pa distributed in the cytoplasm with weak red fluorescence; The MIX group showed combined distribution patterns of free Pa and DOX, that is, DOX was mainly in the nucleus and Pa distributed in the cytoplasm. As a nanoformulation, Doxil exhibited different subcellular behaviors to its parent drug (DOX), showing relatively weaker fluorescent signal and mostly distributed in the cytoplasm. In comparison, PD NPs and PDR NPs showed similar subcellular distribution with DOX spreading from cytoplasm to nucleus and Pa staying in the cytoplasm. Both fluorescences of Pa and DOX showed a sizeable overlapping area with lysosomes, demonstrating that PD NPs and PDR NPs can take advantage of the acidic pH and release the Pa and DOX in lysosomes. In addition, the PD NPs and PDR NPs both showed higher intracellular drug concentrations than the free drugs.

Phototherapy and the immunogenic cell death effect.

Phototherapy can make tumor cells undergo ICD, thus eliciting a robust immune response. As a chaperone protein, calreticulin (CRT) is normally located in the endoplasmic reticulum (ER) that is evenly distributed in the cytoplasm. When ICD happens, CRT will be transported to the cell surface in response to the ER stress, which is considered as another indicator of ICD [32,33]. To prove whether our nanoplatform can induce ICD, PDR NPs and the control materials were incubated with UPPL cells. The location of CRT was stained by immunofluorescence and observed by CLSM. As shown in Fig. 3a, CRT in the PBS-treated group was evenly distributed in the cytoplasm, while in the DOX and PDR NPs treated cells, the CRT was distributed intracellularly with minor changes compared to PBS control. Then, phototherapy was applied. The CRT in PD NPs + L and PDR NPs + L groups were both distributed in the vicinity of the cell membrane, indicating that the phototherapeutic effect of PD and PDR NPs can effectively induce the ICD in UPPL cells.

DC maturation promoted by R837.

DCs are derived from hematopoietic bone marrow progenitor cells, which initially transform into immature DCs (iDCs). iDCs exhibit low T-cell activation ability. Once iDCs contact the surrounding antigens or are stimulated by some immunoadjuvants, such as TLR or STING agonist, they can be stimulated into the mature state (mDCs). mDCs then migrate to lymph nodes and present TAA on major histocompatibility complex (MHC). Meanwhile, co-stimulators, such as CD80 and CD86 on the surface of mDC, are upregulated, which provide co-stimulatory signals during T cell priming and activation [34,35]. The upregulated level of CD86 is a typical marker of DC maturation. Firstly, we evaluated the functionalities of TLR agonist (R837). We incubated equivalent concentrations of free R837, PD NPs and PDR NPs with DC cells (DC2.4), and evaluated the CD80 and CD86 levels on DCs by qPCR. As shown in Fig. 3b and c, the R837-treated cells can significantly upregulate the expression of CD80 and CD86 in comparison to the non-treated control. The PD NPs didn't show noticeable upregulation to the CD80 and CD86 levels due to the lack of R837. The PDR NPs showed the best promotion efficiency to DC cells, as the CD80 and CD86 level was significantly more than all the other three groups. This can be ascribed to the advantages of nanoformulation, which largely improves the bioavailability of the hydrophobic R837. Tumor necrosis factor (TNF) is a well-known maturation and survival factor of DC. As determined by RT-PCR, the R837 and PDR NPs treated UPPL cells both showed significant TNF-α elevation compared to the PBS-treated cells (Fig. 3d), indicating that R837 can effectively promote DC maturation.

Photo-induced STING effect of PDR NPs.

We posited that the powerful phototherapeutic effect of PDR NPs was able to ablate the tumor cells and expose genomic DNA fragments for the STING pathway activation. Here, the Pa-containing nanoformulations (PD and PDR NPs) were incubated with UPPL cells, the photo-induced DNA damage was stained by pico488 and observed under CLSM (Fig. 4a). PD NPs and PDR NPs without light treatment showed similar DNA staining patterns when compared to the PBS control group, indicating that the chemotherapy (PD NPs) and chemo-/immuno-therapeutic effect (PDR NPs) didn't cause apparent DNA damage. In striking contrast, the PD NPs + L and PDR NPs + L groups displayed strong fluorescence in the cell nucleus. Some cells were also stained outside of the nucleus (pointed by red arrows), demonstrating that the phototherapy can effectively induce DNA fragmentation of tumor cells, which may further trigger the STING pathway. To prove this point, we collected the cell culture medium of the PD NPs, PDR NPs, PD NPs + L and PDR NPs + L treated cells, and incubated them with DCs, respectively. The downstream cytokine level was evaluated. The cell lysate of the light-treated groups significantly stimulated the IFN-β expression, and this effect could be enhanced with the prolonged incubation time (Fig. 4b and c). The CXCL 10 level also showed a similar light-related manner (Fig. 4d), supporting that the phototherapy could trigger the STING pathway. To further elaborate on the mechanism, we investigated the protein level downstream of the STING pathway. In the Western blot results (Fig. 4e), the light-treated groups, including PD NPs + L and PDR NPs + L, increased the phosphorylation of the IRF3 and TBK1, which were entirely consistent with the STING activation of cGAMP, a standard STING agonist. All results above strongly support our hypothesis of phototherapy-induced STING activation.

The combinatorial effect of PDR NPs for DC maturation.

We then designed a transwell experiment to mimic the TIME to evaluate the combinatorial effect of ICD, TLR and STING for DC maturation in PDR NPs. As shown in Fig. 4f, UPPL cells were incubated with PD NPs or PDR NPs in the upper chamber and treated with light for 3 min. The treated cells in the upper chamber were further incubated with iDCs (DC2.4 cells) in the lower chamber for another 12 h. The released R837, TAA and DNA fragments can diffuse to the lower chamber and be ingested by iDCs. To evaluate the population of mDCs, CD86 was employed as a marker for the FACS analysis (Fig. 4g and Fig. S9). As control groups, PBS and PBS plus light only showed less than 4% of CD86+ DCs. The PD NPs also showed a similar level of CD86+ DCs to the PBS-treated groups, due to the lack of either PTT or R837 stimulation. When we applied light to PD NPs-treated cells, the population of mDC surged to 13%, indicating that the photo-induced STING and ICD pathways were activated. PDR NPs significantly polarized more iDC to mDC than the PD NPs, demonstrating that the R837-triggered TLR7 worked. Since the mDC population stimulated by PD NPs + L was considerably more significant than the PDR NPs treated group, we speculated that the photo-induced STING and ICD pathways played a synergistic role in the DC maturation. PDR NPs + L was supposed to exhibit the most substantial immunostimulatory effect, as they can activate TLR, STING and ICD pathways simultaneously. As expected, the mDC polarized by PDR NPs + L was much higher than any of the other five groups. These results demonstrated that our nanoplatform showed a combinatorial “3-in-1″ effect on DC maturation via variable pathways. The strong mDC promotion is critical to the subsequent immunotherapy.

Tumor accumulation and biodistribution of PDR NPs.

Then, we investigated whether the PD NPs could effectively deliver the R837 into tumor site. Herein, PDR NPs were i.v. administered into tumor-bearing mice to determine the biodistribution. Since the loading of R837 may cause differences in physiochemical properties of PD NPs (PDR NPs vs PD NPs), we set PD NPs treated mice as control to see if the loading of R837 affect the tumor accumulation of nanoparticles. PDR NPs showed excellent tumor selectivity as PD NPs did (Fig. 5a and b); they preferentially accumulated at the tumor site starting at 2 h, and lasted for more than 48 h. Then, we sacrificed the mice and collected the main organs and tumors to evaluate the biodistribution. PDR NPs showed the highest signal at the tumor sites, and the liver and kidneys also captured some nanoparticles, which is quite similar to PD NPs. In the quantitative analysis of the in vivo and ex vivo imaging (Fig. 5c and d), PDR NPs showed the highest accumulation at tumors at 24 h. The PDR NPs accumulation at the tumor site was significantly higher than the other organs, demonstrating that PD NPs could deliver the R837 to accumulate to the tumor site, which would greatly benefit tumor treatment.

Pharmacokinetics profile of free R837 and encapsulated R837 (PDR NPs).

The high hydrophobicity of R837 (LogP is 2.83 from ALOGPS) would extensively impair blood circulation and bioavailability. As a transformable nanoplatform, the PD NPs were supposed to encapsulate R837 and make it well-suspend in the aqueous circumstance, thus prolonging blood circulation. Hence, the pharmacokinetic profile of free 837 and encapsulated R837 (PDR NPs) were investigated. As shown in Fig. 5e, the PDR NPs could extensively improve the PK of R837. In comparison, the AUC of R837 could be improved 6.6 times from 12.5 to 82.6, and the half-life time ($T_{1/2}$) of R837 can be prolonged 2.4 times from 0.7 h to 1.7 h in the PDR NPs. The better PK profiles of encapsulated R837 supported that the PDR NPs may be able to effectively improve the in vivo performance of R837 and bring benefits to its anti-tumor efficacy.

In vivo photothermal effect of PDR NPs.

Since the PDR NPs could effectively accumulate in the tumor site, the phototherapeutic effect would be significantly improved. To determine whether PDR NPs could be used for phototherapy in vivo, PDR NPs and the control materials were i.v. injected into UPPL tumor-bearing mice respectively. The tumors were irradiated by 680 nm laser (0.6 w/cm^2, 3 min) at the 24 h post-injection (determined by the timepoint of maximum tumor accumulation in Fig. 5a). We used a thermal camera to monitor temperature changes at the cancer sites. As shown in Fig. 5f, Doxil and R837 didn't show any photo-induced hyperthermia compared with PBS control due to the lack of photosensitizer. Both PD NPs and PDR NPs exhibited a strong photothermal effect which elevated the local temperature extensively. The local hyperthermia treatment would effectively ablate the tumor tissue without hurting other normal organs, as the phototherapy only affects the laser-directed region.

In vivo efficacy and distant tumor treatment of PDR NPs.

To investigate the anti-tumor effect of PDR NPs in vivo, UPPL cells were inoculated to the two flanks of C57 mice (female, 6-week-old) to establish tumor-bearing mice. The right tumor was treated with a laser to act as the primary tumor, and the left tumor was considered as distant tumor to evaluate the abscopal effect (Fig. 5g). The animal treating strategy was summarized in Fig. 5h. When the subcutaneous bladder tumors developed to 100 mm^3 in two weeks of the tumor inoculation, treatments started with i.v. injection of different formulations. Besides PDR NPs, we also employed other interventions as controls, such as Doxil, R837, PD NPs. Doxil is a commercial nanoformulation of DOX with better pharmacokinetics than DOX; free R837 was employed to exert immunotherapeutic effect alone; As theranostic nanomedicine, PD NPs presented highly efficient chemotherapy without laser, and synergistic photo-/chemo-therapies and immunotherapy (ICD and STING) with laser treatment. PDR NPs exerted a combination of chemotherapy and immunotherapy (TLR pathway) without laser treatment and multiple therapeutic effects with laser treatment, including phototherapy, chemotherapy and immunotherapy mediated by ICD, TLR and STING pathway. To preclude if the laser exposure also elicited immune response, the mice that were treated with PBS, Doxil and R837 were also irradiated with laser even without any photosensitizer involved. Here, we applied the laser to the right tumor while sparing the left tumor as distant tumor to evaluate the abscopal effect of immunotherapy. In animal treatments (n = 8), we applied three doses of all materials followed by two laser treatments at 24 and 48 h after each injection. The laser dose was set at 0.6 w/cm^2 for 3 min. As shown in Fig. 5i, bladder cancer was highly malignant, tumor mass of PBS-treated mice increased rapidly on both the primary tumor and distant tumor, indicating that laser exposure didn't affect the progress of the primary and distant tumor if no photosensitizer was involved. The R837+L and Doxil + L groups showed slightly better efficacy than the PBS + L treated group, because of the immunotherapeutic effect of R837 and chemotherapeutic effect of Doxil. The PD and PDR NPs both showed similar efficacy to the Doxil-treated mice on both primary and distant tumors. With laser treatment, the PD NPs + L and PDR NPs + L both ablated the primary tumor effectively. The PDR NPs showed better tumor ablation than PD NPs in the last few days, which can be ascribed to the contributions of R837 in PDR NPs. For the distant tumor, PD only showed marginal improvement and PDR NPs demonstrated slightly more potent efficacy, but did not reach a statistical difference. By statistics, PDR NPs + L showed higher efficacy than all the other treatments, indicating that photo-/chemo-/immuno-therapies worked together and induced the abscopal anti-tumor effect. All the groups didn't negatively affect the body weight (Fig. 5j), indicating that our treatments were biocompatible.

Cytotoxic T lymphocytes (CTL) are one of the most important immune cells for cancer treatment. They release perforin and granzyme to kill cancer cells directly. During the immune response, immune cells are negatively regulated through signaling of immune checkpoints, such as the PD1/PD-L1 pathway, to prevent overly reactive immune response. Cancer cells hijack this normal regulatory pathway, express PD-L1 and suppress anti-cancer CTLs. As shown in Fig. 5i, the PDR NPs + L can inhibit the growth of the distant tumor significantly compared to the other treatments, but not in a highly efficient way. PD NPs + L and PDR NPs groups only exhibited slight efficacy to the distant tumors. We posit that T cells may not recognize tumor cells due to the PD-1/PD-L1 pathway. Herein, we set up new animal experiments with PD-1 antibody. Besides the drug treatment plus laser irradiation, α-PD1 (200 µg/mouse) was i.p. administered twice a week for two consecutive weeks along [36,37]. We set 6 groups for the animal experiments, including PBS + L, Doxil + L+α-PD1, R837+L+α-PD1, PDR NPs+α-PD1, PD NPs + L+α-PD1 and PDR NPs + L+α-PD1. As shown in Fig. 5k, all treatment groups exhibited excellent anti-cancer effects compared to the PBS + L group, among which PDR NPs + L+α-PD1 and PD NPs + L+α-PD1 exhibited the best tumor ablation effects. In these two groups, all the primary tumors were completely ablated. The Doxil + L+α-PD1 and R837+L+α-PD1 groups also showed better efficacy than the treatments without α-PD1, demonstrating that immunotherapy played a significant role in cancer treatment. In the distant tumor, PDR NPs + L+α-PD1 extensively slowed down the tumor progression, suggesting the best abscopal effect. PD NPs + L showed less efficacy than the PDR NPs + L did. The other three groups, including Doxil + L+α-PD1, R837+L+α-PD1, PDR NPs+α-PD1 also showed some extent of the abscopal effect, but all significantly weaker than PDR NPs + L+α-PD1 did. All the groups with α-PD1 didn't negatively affect the body weight (Fig. 5l), indicating that our treatments were nontoxic. These results demonstrated that PDR NPs in combination with α-PD1 not only ablated the primary tumor, but also effectively slowed down the metastatic tumor development due to the excellent photo-/chemo-/immuno-therapies.

The phototherapeutic effect of PDR NPs.

The tumor conditions after PTT treatment were analyzed by histopathology. As shown in Fig. 5m, the tumor tissues of PD and PDR NPs were both intact if no laser treatment was involved, while apparent tissue damage was observed in the laser-treated groups, indicating that powerful PTT effects of PD and PDR NPs could efficiently ablate the tumors.

The immune system regulation of the nanoplatform.

Cytotoxic T lymphocytes (CD3$^+$CD4$^-$CD8$^+$) and helper T cells (CD3$^+$CD4$^-$CD8$^+$) are the major players in the regulation of adaptive immunities. To investigate the immune regulatory capabilities of our nanoplatforms, the populations of the cytotoxic T lymphocytes and helper T cells were further profiled. We sacrificed the mice and collected the distant tumor at Day 40 for the FACS analysis. Fig. 6a&6b and Fig. S10 showed the populations of CD8$^+$ and CD4$^+$ T cells in different groups. The Doxil+α-PD1 and R837+α-PD1 significantly increased the populations of both CD8$^+$ and CD4$^+$ T cells compared to the PBS + L treated group, indicating that these two treatments elicited a considerable immune response in tumors. Compared to the groups treated with Doxil+α-PD1 and R837+α-PD1, the PD NPs + L+α-PD1 group recruited significantly more CD8$^+$ T cells, but no significant difference in CD4$^+$ T cells. The mice treated with PDR NPs showed fewer CD8$^+$ T cells in tumors than PD NPs + L+α-PD1. Among all these treatments, PDR NPs + L+α-PD1 exhibited the most potent effect on the recruitment of both CD8$^+$ and CD4$^+$ T cells owing to the combinatorial activation effect of the STING, ICD and TLR pathway. Such excellent "3-in-1″ immunotherapies can explain the reasons why PDR NP + L treated mice showed the best abscopal effect. Immunosuppressive CD4$^+$ FoxP3+ Treg cells can broadly dampen the immunotherapy. As shown in Fig. 6c and Fig. S11, the PBS groups showed the highest level of the Treg population. When we added other therapeutic agents, including Doxil, R837, PD NPs and PDR NPs, the population of the Treg cells decreased, indicating that our nanoplatform could promote the anti-tumor immunity and downregulate the immunosuppressive cells.

To further investigate the TIME regulated by our nanoplatforms, M2 type TAM, Treg cells and CD8$^+$ T cells were evaluated by immunohistochemistry (IHC). As shown in Fig. 6d, the PBS-treated tumor showed the highest level of the Ki67 positive cells; R837 and Doxil-treated tumors both displayed a high level of Ki67 expression, which was highly consistent with the anti-tumor results in Fig. 5k. In comparison, PD NPs + L, PDR NPs and PDR NPs + L vastly slowed down tumor proliferation and with the lowest Ki67 expression. Immunosuppressive M2 type TAMs were at the lowest level in PDR NPs + L treated group, and highest in the PBS and Doxil treated groups. Treg (FoxP3) and CD8 marker expressions were consistent with FACS results. PDR NPs + L showed the highest level of the CD8$^+$ cells, and also higher in the others than the PBS treated mice. For the FoxP3+ cells, the PBS-treated mice showed the highest level. The other groups showed fewer T-reg cells, indicating that all these treatments could regulate the immunosuppressive TIME. All these data supported that our nanoplatforms could effectively regulate the immunosuppressive TIME for the anti-tumor effect.

Toxicity evaluation of the nanoplatform.

PDR NPs and PD NPs mainly accumulated in tumor sites other than in normal organs (Fig. 5a to b), and therefore, is less likely to cause damage to normal organs. To prove the biocompatibility of our nanoplatforms, we collected major organs, including the heart, liver, spleen, lung and kidney for histopathological examination. As shown in Fig. S12, no visible damage was observed in any of the normal organs when compared to the PBS-treated group. We also studied the impact of DOX at a high dose (10 mg/kg). As shown in Fig. S13, free DOX significantly reduced the counts of whole blood cells, lymphocytes, monocytes and granulocytes, indicating its detrimental effects on immunotherapy. In contrast, both PD NPs and PDR NPs (20 mg/kg) didn't affect these blood cell counts. The H&E and blood analysis results indicated that our nanoplatforms were safe.

Long-term memory effect of immunotherapy.

Cancer recurrence is the most common cause of treatment failure. One major advantage of immunotherapy is the development of memory immune cells and immune surveillance that can induce long-term remission. To determine anti-cancer immune memory (Fig. 7a), subcutaneous tumors from UPPL cells were removed either by surgery or the strong PTT effect (mediated by PDR NPs) on Day 14, followed by 2 doses of α-PD1 i.p. administration (200 μg/mouse) to the mice on Day 15 and Day 17. The mice were further housed for 36 more days. Then UPPL cells were inoculated back to the mice together with 2 doses of α-PD1 i.p. administration (200 μg/mouse). Fig. 7b–d showed that the newly transplanted tumor grew very fast in mice whose tumors were removed by surgery. In striking contrast, the nanoplatform-treated mice exhibited a strong memory effect that effectively prevented or stopped tumor regression. These treatments didn't show observable side effects as the body weights continued to increase in both groups (Fig. 7e). The newly implanted tumor didn't re-develop in 3 mice (50%). This group showed much longer overall survival, and 3 mice survived more than 110 days (Fig. 7f). In contrast, all the mice dead within 84 days in the surgery group. To better understand the mechanism underlying the anti-recurrence effect of the PDR NPs, the effector memory T cells (T_{EM}, $CD3^+CD8^+CD44^+CD62L-$) in the spleen were examined by using FACS on day 40 prior to the tumor rechallenging inoculation. As shown in Fig. 7g and Fig. S14, PDR NPs plus laser irradiation and α-PD1 significantly increased the population of the T_{EM} in the spleen, comparing to the surgery+α-PD1 treated mice. The changes in T_{EM} were highly consistent with the tumor growth and survival, supporting that our nanoplatform could evoke the immune memory effect to reduce tumor relapse significantly.

3. Conclusions

In this work, we developed a versatile nanoplatform to combine with a TLR7 agonist (R837) for the synergistic photo-/chemo-/immuno-therapies towards advanced cancer. Interestingly, we found that phototherapy can simultaneously evoke ICD and STING pathways, which makes PDR exhibit multiple promising immunostimulatory properties, that is ICD, STING and TLR stimulations. Moreover, multiple therapeutic functionalities, including chemotherapy by DOX, phototherapy by Pa and immunotherapy by ICD, TLR and STING pathway, exhibits a solid anti-tumor effect to treat primary and distant tumors and reduce recurrent tumors. For the primary tumor, the phototherapy contributed more because it directly ablated the tumor mass; as for the distant tumor, the chemotherapy and immunotherapy both contributed. The recurrent tumors were majorly inhibited by immunotherapy as the phototherapy and chemotherapy would not last long. PDR NPs also behaved similarly to the Trojan Horse nanotheranostic, which showed the ideal size and charge transformation that enabled much higher drug delivery efficiency than conventional nanomedicines. Combining these merits, PDR NPs can effectively ablate the primary bladder cancer, suppress the distant tumor and reduce cancer recurrence.

4. Materials and methods

Materials and instruments.

Pheophorbide a was purchased from Santa Cruz Biotechnology Inc; doxorubicin hydrochloride was from BIOTANG Inc; Anhydrous hydrazine and diamine terminated polyethylene glycol 2000 (PEG_{2000}-$2NH_2$) were bought from SINOPEG Inc (Xiamen, China); and Imiquimod (R837) was from Alfa Aesar. All the solvents were bought from commercial sources and used without further purification. The synthesis of PhD monomer was confirmed by electrospray ionization mass spectrometry (ESI-MS, Thermo Electron LTQ-

Orbitrap XL Hybrid) and nuclear magnetic resonance (NMR) spectrometer (600 MHz Avance III, Bruker, Germany). The morphology of PDR NPs was determined by transmission electron microscopy (Talos L120C TEM, FEI) with an acceleration voltage of 90 kV. The size distribution and surface charge of PDR NPs were measured by dynamic light scattering (DLS, Zetasizer Nano ZS, Malvern). UV–vis spectra were obtained by UV–vis spectrometer (UV-1800, Shimadzu). Fluorescence spectra were evaluated by a fluorescence spectrometer (RF-6000, Shimadzu). For the cell viability experiments, the light treatment was carried out by using a near-infrared fluorescent light panel (Omnilux new-U) which can cover a broader area for 96-well plate. The cell distribution and calreticulin expression were captured by a confocal laser scanning microscopy (LSM800, Carl Zeiss). R837 was quantified with a Waters HPLC system with UV–vis detector. The quantifications of DC maturation and T-cell populations were conducted by a BD Fortessa 20 color flow cytometry. The cytokine level was evaluated by RT-PCR.

Synthesis of the building blocks.

For the synthesis of Pa-hydrazide-DOX (PhD) monomer and PEG-2CHO, 1 mmol pheophorbide a (~594 mg), 2 mmol 1-ethyl-3-(3-dimethylaminopropyl) carbodiimide (EDC, 383 mg) and 4 mmol N-hydroxysuccinimide (NHS, 460 mg) were dissolved in 20 mL dichloromethane, and the solution was vigorously stirred in ambient temperature for 30 min to activate the carboxylic acid of pheophorbide a. Then, 6 mmol anhydrous hydrazine (188 μL) was introduced to the reaction system. The reaction was kept stirring for another 4 h at room temperature. The pheophorbide a-hydrazide was purified by extraction (water against dichloromethane). The pheophorbide a-hydrazide was then conjugated with doxorubicin to form PhD monomer. Pheophorbide a-hydrazide and doxorubicin hydrochloride were dissolved in anhydrous methanol with a drop of TFA. The whole reaction system was reflux overnight. PhD monomer was purified by column chromatography.

The PEG-2CHO was synthesized by directly attaching two aldehydes to the termini of PEG$_{2000}$ with two amine groups (PEG-2NH$_2$). In detail, 4-formylbenonic acid (3 mmol), EDC (6 mmol) and NHS (12 mmol) were dissolved in 20 mL dimethylformamide (DMF). The mixture was stirred at room temperature for 30 min. Then, PEG2$_{000}$-2NH$_2$ (0.3 mmol) were added into the reaction system and stirred for another 24 h at room temperature. The resultant PEG-2CHO was precipitated in cold ether and further dialyzed in a dialysis tube (MWCO is 1000 Da).

Preparation of PDR NPs.

PhD monomer (2 mg) and R837 (0.2 mg) were dissolved in THF/methanol (1:3, vol/vol) mixing solvent. Then, the solution was dropped into 1 mL water under vigorous stirring. The whole system was kept under stirring until the organic solvent was completely evaporated at room temperature. Then, the aqueous solution of PEG-2CHO was added to the system to form the final PDR NPs. The free R837 was isolated by centrifugal dialysis (MWCO is 10 kD) and qualified according to a standard curve based on HPLC test. A SunFire C18 analytical column (150 mm, 4.6 mm, 5 μm, Waters) was used to analyze the R837 at 25 °C with an isocratic flow of mobile phase of acetate buffer (pH 3.7) and acetonitrile (50/50, vol/vol). The flow speed was set to 1.5 mL/min. The absorbance of the UV–vis detector was set at 244 nm. The encapsulation efficiency (EE%) was calculated by following the formula: $(W_{\text{loaded drug}}/W_{\text{total drug}})*100\%$; the loading capacity (LC%) was calculated by: $[W_{\text{loaded drug}}/(W_{\text{loaded drug}} + W_{\text{Carrier}}]*100\%$. In the formula, the $W_{\text{loaded drug}} = W_{\text{total drug}} - W_{\text{free Drug}}$.

Optical properties of PDR NPs.

5 μM Pa, PD NPs, PDR NPs and equivalent concentrations of R837 were prepared for measurement of optical property. For UV–vis spectra, the absorbance range was set as 800 nm–220 nm. For fluorescence spectra, the excitation was set as 412 nm, and the emissive band was set from 432 nm to 800 nm. For the measurement of optical property, the path length of the quartz cuvette was 2 mm.

Laser dose determination.

The laser conditions were determined by following a published work which systemically investigated the phototherapeutic effects of porphyrin-based nanoparticles [38] The porphyrin-based nanoparticles mainly exhibited PDT effect at a laser power of 0.2 W, and PTT effect at 0.75 W, respectively. Since we tried to employ both PDT and PTT to treat cancers, the laser power was set to 0.6 W which is in the middle of 0.2–0.75 W. Pre-experiments were conducted to determine the irradiation time; we found that 3 min irradiation was sufficient enough to ablate the subcutaneous tumor after three treating circles (one drug injection + two laser treatments). Hence, the laser dose was set as 0.6 w/cm^2 for 3 min.

Photo-induced hyperthermia and ROS production of PDR NPs. Aqueous suspension of PDR NPs at different concentrations (0 µM, 1 µM, 5 µM, 10 µM, and 50 µM) were placed in a 96-well plate and irradiated with 0.6 w/cm^2 laser (680 nm) for 3 min. The temperature of the nanoparticle suspension was recorded by a FLIR thermal camera. The ROS production of PDR NPs was indicated by a commercial ROS probe, singlet oxygen sensor green (SOSG). Similar to hyperthermia experiments, PDR NPs at different concentrations (0 µM, 1 µM, 5 µM, 10 µM, and 50 µM) were incubated with SOSG and the whole system was irradiated with 680 nm laser (0.6 w/cm^2, 3 min). The fluorescence intensity of the SOSG was monitored by a fluorescence spectrometer to reflect ROS production.

Critical aggregation concentration of PDR NPs.

The critical aggregation concentration (CAC) of PDR NPs was measured by following the same method used for critical micelle concentration (CMC) measurement. Firstly, different concentrations of PDR NPs, including 50 µM 10 µM, 5 µM, 1 µM, 0.5 µM, 0.1, µM, 0.05 µM and 0.01 µM, were prepared and incubated with 0.1 mM pyrene acetone solution at 37 °C for 2 h. The fluorescence of pyrene was tested by using an excitation of 335 nm. The fluorescence intensity of the third peak (I_3) and first peak (I_1) were compared for CAC calculation.

Drug release of PDR NPs.

100 µM PDR NPs were incubated in the solvent with a pH of 7.4 and 5.0 respectively. The samples were then loaded in dialysis bags (MWCO = 7000 Da) for dialysis against distilled water. The samples in the dialysis bag were collected at different time points. The UV–vis absorbance was measured for the quantification of DOX and R837. Since the aims of the drug-releasing test are: i) to check if the PDR NPs released the drugs in a pH-responsive manner; ii) to see if our nanoparticle can release the drug effectively. We monitored the drug release in a limited time which was determined by the timepoint that the drug release tends to go up very slowly, like reaching a plateau.

Stability of PDR NPs.

100 µM PDR NPs were incubated with 10% FBS (fetal bovine serum) and kept at room temperature. The size variations of PDR NPs were monitored by DLS every other day. All the samples were repeated in triplicates.

Dislocation of calreticulin (CRT) by the treatment of PDR NPs. UPPL cells (3 × 10^4 cells per well) were seeded in a µ-slide 4-well microscopy chamber (ibidi GmbH) for 24 h until fully attached. Then, the UPPL cells were treated with 10 µM of DOX, PD NPs and PDR NPs for 4 h. The PD NPs and PDR NPs treated cells were exposed under laser for 3 min. Thereafter, the cells were fixed and permeated with 3.7% paraformaldehyde for 20 min and 0.2% X-Tron for 10 min, respectively. The nucleus was stained with Hoechst 33342 for 10 min. The cell membrane was stained with DiD for 10 min. The CRT expression was stained an Alexa Fluor® 647-conjugated anti-CRT antibody (ab196159, 1/500, Abcam).

DC maturation promoted by PDR NPs.

DC 2.4 cells were seeded in 6-well plate overnight until the cells were fully attached. Then, the cells were treated with 10 µM R837, PD NPs, or PDR NPs for 24 h. To evaluate the maturation of DC, the CD86 and TNF-α level were tested by qPCR. For *in vitro* DC activation experiments of R837, 10^6 of DC 2.4 cells co-cultured with 10 µM R837, PD NPs, or PDR NPs for 24 h. DC 2.4 cells incubated with 50 ng/mL lipopolysaccharide (LPS) were set as positive control. After incubation, the expression of matured DC activation markers was analyzed with a flow cytometer. The cells were stained with Percp/Cy5.5-conjugated anti-CD80 antibody (Clone: 2D10).

DC maturation promoted by a combinatorial effect of ICD, TLR and STING pathways.

UPPL cells were seeded in the upper chamber of the transwell plate overnight to allow the cells fully attached. The UPPL cells received 6 different treatments, including PBS, PBS with light (PBS + L), PD NPs, PD NPs + L, PDR NPs and PDR NPs + L for 3 h. The light-treated groups were exposed under a laser panel for 3 min. Then, the treated UPPL cells were incubated together with the DC cells that have been seeded in the lower chamber. The whole chamber plate was placed in the incubator for another 20 h to allow the materials in the upper chamber traveling to the low chamber and stimulating the DC2.4 cells. The DC2.4 cells were collected and stained with Percp/Cy5.5-conjugated anti-CD80 antibody (Clone: 2D10) for the flow cytometry analysis.

Elevated cellular uptake of PDR NPs under slightly acidic pH.

10 μM PDR NPs were incubated with $6*10^5$ UPPL cells in cell culture medium with different pH (7.4 and 6.5), respectively. After 2 h incubation, the cells were washed with PBS to remove the PDR NPs containing medium and maintained in PBS. Then, $5*10^5$ cells were collected and dissolved in DMSO for fluorescence test. The fluorescence of DOX was measured to compare the cellular uptake between the PDR NPs in pH 7.4 and 6.5. The experiments were repeated in triplicates.

Cell spheroid penetration of PDR NPs.

UPPL cells were seeded in a round-shape bottom plate at a density of 10^5 per well for spheroid formation. After 48 h incubation, the cell spheroids were treated with PDR NPs in a cell culture medium with different pH (7.4 and 6.5) for 24 h. The cell spheroids were then washed with PBS three times to remove the PDR NPs contained medium and maintained in PBS. The cell spheroids were applied to CLSM observation immediately without fixing, the Z-axis was kept at the same depth during the CLSM scanning between the groups. The distribution of DOX was employed to indicate the penetration of PDR NPs. The FITC channel was employed to observe DOX in spheroids. The incubating concentration of PDR NPs was calculated based on the equivalent molar concentration of 5 μM DOX.

Cell viability investigation.

UPPL bladder cancer cells and human umbilical vein endothelial cells (HUVECs) were seeded in 96-well plate with a density of 6000 cells per well, respectively. The cells were incubated overnight until fully attached. Then, the cells treated with PDR NPs and control materials, including PD NPs, free Pa, free DOX, free R837, a physical mix of Pa, R837 and DOX, nanoformulation of DOX (Doxil). The materials that contained Pa, including free Pa, MIX, PD NPs and PDR NPs, were applied to light treatment. The materials were firstly incubated with UPPL cells for 12 h, then washed away by PBS and replaced by fresh medium. The light-treated groups received 3 min light treatment, and cells were incubated in the incubator for another 12 h. The non-light treated groups followed the same procedures, except for the light treatment. The cell viability was analyzed by MTT assay.

Cell distribution of PDR NPs.

PDR NPs and control materials with intrinsic fluorescence, such as DOX, Pa, MIX, Doxil and PD NPs, were incubated with UPPL cells for subcellular distribution observation. The cells were incubated with these materials for 4 h, then washed with PBS for three times. The cells were maintained in PBS and applied to CLSM observation immediately without fixing. The fluorescence signal of DOX or Pa was observed by CLSM. The lysosomes were indicated by LysoTracker Green. All the materials were calculated based on the equivalent molar concentration of 5 μM DOX.

The phototherapeutic effect of PDR NPs.

UPPL cells were seeded in glass-bottom dishes and treated with 10 μM PD NPs and PDR NPs for 2 h, respectively. The cell culture medium was washed off by PBS and replaced with fresh medium. The cells were exposed under 680 nm laser (0.6 w/cm^2) for 3 min and stained with DiOC6(3) to indicate the live cells, and propidium iodide (PI) for 20 min to label the dead cells. The stained cells were observed by CLSM.

Conditional medium collected.

5×10^5 UPPL cells were seeded in a 6-well plate overnight to allow cells fully attached. The UPPL cells were treated with PD NPs and PDR NPs for 24 h, and the nanoparticle-contained medium was replaced with fresh cell culture medium. The PD NPs or PDR NPs treated UPPL cells were applied to light exposure for 5 min and cultured for another 24 h. Then, the cell culture medium was collected for the centrifugation (2000 rpm for 3 min). The supernatant was collected as the conditional medium after discarding the cell debris.

Immunoblotting analysis.

Immunoblotting analysis was performed as previously described [39]. Briefly, THP-1 cells were treated with different conditional medium for 2 h. The treated THP-1 cells were harvested and lysed in RIPA buffer (Thermo Fisher). Cell lysates were resolved by SDS-PAGE before transferring to PVDF membranes. PVDF membranes were incubated with 5% non-fat dry milk in TBST buffer for 1 h at 37 °C to block nonspecific protein binding. Primary antibodies (1:1000), including p-IRF3/p-TBK1 (Cell Signaling Technology, InC), IRF3 (Proteintech Group, Inc.) TBK1 (ABclonal Technology, Inc.), were diluted in a washing buffer containing 5% BSA and applied to the PVDF membranes overnight at 4 °C. After extensive washing, the PVDF membranes were incubated with peroxidase-conjugated antibodies for 1 h at room temperature and washed again. Immunoreactive bands were visualized using a ChemiDoc™ MP imaging system.

qPCR assay.

THP-1 cells were treated with the PD NPs or PDR NPs related conditional medium for 2 h, then the cells were collected for the RNA analysis. The total RNA was isolated by the TRIZOL reagent (Invitrogen) and the phenol-chloroform extraction method according to the manufacturer's instruction. The cDNA was synthesized by the SuperScript reverse transcriptase (Invitrogen) with 2 µg total RNA. qPCR was carried out with SYBR Green PCR Master Mix (Thermo Fisher) on a CFX96 Real-Time PCR Detection System (Bio-Rad). GAPDH was used to normalize the level of mRNA expression. The qPCR primers were synthesized by Integrated DNA Technologies, Inc. The corresponding sequences are: IFN-beta: Forward:5-AAGGAGGACGCCGCATTG-3 Reverse:5- CCAGGACTGTCTTCAGATGCT-3; CXCL10: Forward:5-TGGCATTCAAGGAGTACCTC-3 Reverse: 5-TTGTAGCAATGATCTCAA-3; IL6: Forward:5-GGTACATCCTCGACGGCATCT-3 Reverse:5-GTGCCTCTTTGCTGCTTTCAC -3; GAPDH: Forward:5-GGAGCGAGATCCCTCCAAAAT-3 Reverse:5-GGCTGTTGTCATACTTCTCATGG-3.

IFN Induction by THP-1 reporter assay.

1×10^6 THP-1 dual reporter cells (InvivoGen) were incubated with a conditional medium for 24 h. Then, Prepare QUANTI-Luc™ (InvivoGen) following the instructions on the enclosed datasheet. Pipet 50 µL of sample per well into a 96-well white plate. Add 50 µl of QUANTI-Luc™ assay solution to each well or tube. Gently tap the plate several times to mix (do not vortex). Proceed immediately with the measurement by luminescence (SpectraMax iD5).

DNA damage image assay.

2×10^4 UPPL cells were seeded in a culture dish with glass bottom plate (Greiner Bio-One) overnight and treated with 10 µM PD and PDR NPs for 24 h, respectively. Cells were washed with PBS and with or without light exposure for 5 min pico488 (Lumiprobe) were added to each well and further incubated for 4 h, CLSM was employed to monitor the DNA stain in cells.

Animal experiments.

The mouse model of bladder cancer was employed, as phototherapy is feasible for bladder cancer, and the tumor growing on the bladder is light reachable if using a light catheter. Although the orthotopic model of bladder cancer was not employed here, the proof-of-concept experiments encouraged us to study orthotopic models in the future further. All animal experiments were strictly in compliance with the guidelines of Animal Use and Care Administrative Advisory Committee (IACUC) of the University of California, Davis and Shanghai Jiao Tong University.

PDR NPs induced lymphopenia.

DOX, PD NPs and PDR NPs were i.v. injected into C57BL/6 mice (n = 3). PBS solution was i.v. injected as control. The blood of the treated mice was collected for the blood chemistry analysis in 24 h. The concentration of the materials was calculated based on the equivalent dose of 10 mg/kg DOX. The treating dose of PD NPs and PDR NPs were 20 mg/kg, respectively.

Biodistribution of PDR NPs.

10^6 UPPL cells were inoculated subcutaneously to the C57BL/6 mice. The xenograft tumors developed with a size of 100 mm^3 in two weeks. Then, 5 mg/kg PDR NPs were i.v. administered to the tumor-bearing mice (n = 3). Equivalent concentrations of PD NPs were employed as control. The near-infrared fluorescence (NIRF) of Pa in tumor-bearing mice was monitored by an animal imaging system at different timepoints. After the whole-body imaging, all the mice were sacrificed for *ex vivo* imaging, the tumors and major organs, including heart, liver, spleen, lung, kidneys, small intestine, muscle and skin, were collected for NIRF imaging.

Pharmacokinetics evaluation of R837 and PDR NPs (PD NP@R837).

Sprague–Dawley rats (male, n = 3) were i.v. injected with equivalent amounts of R837 and PDR NPs, respectively. The highly hydrophobic R837 was dissolved in a Cremophor EL/ethanol mixture. The treatment dose of free R837 was 1 mg/kg and the PDR NPs was 10 mg/kg which encapsulated 10% R837. Whole blood samples (~50 µL) were collected from the rat tail at predetermined time points post-injection. The whole blood samples were then centrifuged for serum collection; then the blood serum was extracted by chloroform against water. The R837 that remained in chloroform was dried and dissolved in acetonitrile for HPLC analysis. A SunFire C18 analytical column (150 mm, 4.6 mm, 5 µm, Waters) was used to analyze the R837 at 25 °C with an isocratic flow of mobile phase of acetate buffer (pH 3.7) and acetonitrile (50/50, vol/vol). The flow speed was set to 1.5 mL/min. The absorbance of the UV–vis detector was set at 244 nm. The area under the curve (AUC) and half-life time ($T_{1/2}$) were calculated by Prism 8.

Establishment of animal models and the treatments procedure.

The mouse model with xenograft bladder tumor was established by inoculating 1×10^6 UPPL cells to two sides of the flanks of C57BL/6 mice (n = 8, female, 6-week-old). The xenograft tumors were developed with a size around 100 mm^3 within two weeks; then the mice were randomized into different groups for the treatments. The materials, including PBS, Doxil, R837, PD NPs and PDR NPs, were i.v. administered to the mice once per week for consecutive 3 weeks. The laser treatment was applied at 24 h and 48 h right after the material administration. The timing of laser irradiation was determined based on animal imaging results. The tumors on the right side were treated with laser (0.6 w/cm^2 for 3 min). The tumors on the left side were considered distant tumors and didn't receive laser treatment. Meanwhile, the tumor size and body weight were recorded along with the whole treatment. For the new animal experiments that combined the materials with immune checkpoint blockade (α-PD1), the tumor-bearing mice were established following the same procedure as aforementioned. The α-PD1 (200 µg/mouse) was i.p. administered weekly for two consecutive weeks starting at first does of the materials. The dose of PDR NPs was 10 mg/kg (based on the PhD monomer). The doses of Doxil, R837, PD NPs were calculated equivalently to PDR NPs.

Photothermal effects of PDR NPs.

PDR NPs and the control materials were i.v. injected into UPPL bladder tumor-bearing mice (n = 6). 24 h after the materials treatments, the tumors were exposed to 0.6 w/cm^2 laser (680 nm) for 3 min, the laser-induced hyperthermia on the tumor site was monitored by using a FLIR thermal camera. The dose of PDR NPs was 10 mg/kg (based on the PhD monomer). The doses of control materials were calculated equivalently to PDR NPs.

T cells quantification by FACS.

The populations of T cells, including cytotoxic T lymphocytes (CTL, $CD3^+CD8^+CD4^-$), helper T cells (Th, $CD3^+CD4^+CD8^-$) and regulatory T cells (Treg, $CD3^+CD4+Foxp3+$), were quantified by FACS. The distant tumors in different groups were harvested from the mice, the tumor tissues were cut into small pieces and homogenized into single cell in PBS contained with 2% FBS. The red blood cells (RBC) were removed by using RBC lysis buffer. The single cell suspensions were stained with Brilliant Violet 785™ anti-human CD3 Antibody (BioLegend, Inc., Clone: OKT3, Catalog no: 317330), Brilliant Violet 605™ anti-mouse CD8a Antibody (BioLegend, Inc., Clone: 53-6.7, Catalog no: 100744), Brilliant Violet 711™ anti-human CD4 Antibody (BioLegend, Inc. Clone: OKT4, Catalog no: 317440) and Alexa Fluor® 488 anti-mouse FOXP3 Antibody (BioLegend, Inc., Clone: MF-14, Catalog no: 126406) by strictly following the manufacturer's protocols. The CTL cells were analyzed as $CD3^+CD8^+CD4^-$cells, Th cells were analyzed as $CD3^+CD4^+CD8$, and Tregs are $CD3^+$CD4+Foxp3+.

IHC and H&E stain.

At the endpoint of animal treatments, the distant tumor on the left-side were collected for IHC analysis. The tumor tissues were sliced and stained by different antibodies, such as these for the indication of Treg cell (FOXP3+), CTL ($CD8^+$), M2 TAM (CD163+) and tumor proliferation (ki67). Meanwhile, the tumor tissues were also prepared for the H&E stain to evaluate the biocompatibility of PDR NPs and the control materials. For the photothermal induced tissue rupture H&E stain, the laser-treated tumor was used.

Tumor relapse prevented by PDR NPs.

1×10^6 UPPL cells were inoculated to the flank of C57BL/6 mice (n = 6) to establish a bladder tumor-bearing mouse model. The subcutaneous UPPL tumors were removed either by surgery or the strong PTT effect (mediated by PDR NPs) on Day 14, followed by two doses of α-PD1 i.p. administration to the mice on Day 15 and Day 17. The mice were further housed for 36 more days. Then UPPL cells were then inoculated back to the mice together with two doses of α-PD1 i.p. administration. The size of the newly inoculated tumor was monitored; the bodyweight of the mice was recorded in the meantime. The animal survival was determined by the tumor volume after the treatment. The endpoint was determined if the tumor volume is larger than 1500 mm^3 (mice would be considered dead) or a mouse was actually dead. The dose of PDR NPs was 10 mg/kg (based on the PhD monomer).

Evaluation of the mechanism underlying the anti-recurrence effect.

1×10^6 UPPL cells were inoculated to the flank of C57BL/6 mice (n = 3) to establish a bladder tumor-bearing mouse model. The subcutaneous UPPL tumors were removed either by surgery or the strong PTT effect (mediated by PDR NPs) on Day 14, followed by two doses of α-PD1 i.p. administration (200 µg/mouse) to the mice on Day 15 and Day 17. The mice were further housed for 36 more days and sacrificed to analyze effector memory T cells (T_{EM}). The population of T_{EM} ($CD3^+$ $CD8^+$ CD62L- $CD44^+$) in spleen was qualified by FACS.

Statistical Analysis.

The data statistics were analyzed by Prism GraphPad software. t-test was employed for comparison of two groups; one -way ANOVA was used for multiple groups. All the results were provided as mean ± s.d.

References

1 S.D. Allen, X. Liu, J. Jiang, Y.-P. Liao, C.H. Chang, A.E. Nel, H. Meng Immune checkpoint inhibition in syngeneic mouse cancer models by a silicasome nanocarrier delivering a GSK3 inhibitor Biomaterials, 269 (2021), Article 120635

2 F. Wang, H. Su, D. Xu, M.K. Monroe, C.F. Anderson, W. Zhang, R. Oh, Z. Wang, X. Sun, H. Wang, F. Wan, H. Cui Therapeutic supramolecular tubustecan hydrogel combined with checkpoint inhibitor elicits immunity to combat cancer Biomaterials, 279 (2021), Article 121182

3 M. Chen, R. Chen, Y. Jin, J. Li, X. Hu, J. Zhang, J. Fujimoto, S.M. Hubert, C.M. Gay, B. Zhu, Y. Tian, N. McGranahan, W.-C. Lee, J. George, X. Hu, Y. Chen, M. Wu, C. Behrens, C.-W. Chow, H.H.N.

Pham, J. Fukuoka, J. Wu, E.R. Parra, L.D. Little, C. Gumbs, X. Song, C.-J. Wu, L. Diao, Q. Wang, R. Cardnell, J. Zhang, J. Wang, X. Le, D.L. Gibbons, J.V. Heymach, J. Jack Lee, W.N. William, C. Cheng, B. Glisson, I. Wistuba, P. Andrew Futreal, R.K. Thomas, A. Reuben, L.A. Byers, J. Zhang Cold and heterogeneous T cell repertoire is associated with copy number aberrations and loss of immune genes in small-cell lung cancer Nat. Commun., 12 (1) (2021), p. 6655

4 J. Galon, D. Bruni Approaches to treat immune hot, altered and cold tumours with combination immunotherapies Nat. Rev. Drug Discov., 18 (3) (2019), pp. 197-218

5 H. Dai, Q. Fan, C. Wang Recent applications of immunomodulatory biomaterials for disease immunotherapy Explorations, 2 (6) (2022), Article 20210157

6 G.N. Barber STING: infection, inflammation and cancer Nat. Rev. Immunol., 15 (12) (2015), pp. 760-770

7 X. Sun, Y. Zhang, J. Li, K.S. Park, K. Han, X. Zhou, Y. Xu, J. Nam, J. Xu, X. Shi, L. Wei, Y.L. Lei, J.J. Moon Amplifying STING activation by cyclic dinucleotide–manganese particles for local and systemic cancer metalloimmunotherapy Nat. Nanotechnol., 16 (11) (2021), pp. 1260-1270

8 Q. Ni, F. Zhang, Y. Liu, Z. Wang, G. Yu, B. Liang, G. Niu, T. Su, G. Zhu, G. Lu, L. Zhang, X. Chen A bi-adjuvant nanovaccine that potentiates immunogenicity of neoantigen for combination immunotherapy of colorectal cancer Sci. Adv., 6 (12) (2020), Article eaaw6071

9 S. Adams Toll-like receptor agonists in cancer therapy Immunotherapy, 1 (6) (2009), pp. 949-964

10 A. Marcus, A.J. Mao, M. Lensink-Vasan, L. Wang, R.E. Vance, D.H. Raulet Tumor-derived cGAMP triggers a STING-mediated interferon response in non-tumor cells to activate the NK cell response Immunity, 49 (4) (2018), pp. 754-763.e4

11 X. Cai, Y.-H. Chiu, Zhijian J. Chen The cGAS-cGAMP-STING pathway of cytosolic DNA sensing and signalling Mol. Cell, 54 (2) (2014), pp. 289-296

12 Q. Chen, J.W. Chen, Z.J. Yang, J. Xu, L.G. Xu, C. Liang, X. Han, Z. Liu Nanoparticle-enhanced radiotherapy to trigger robust cancer immunotherapy Adv. Mater., 31 (10) (2019), Article 1802228

13 Q. Chen, L.G. Xu, C. Liang, C. Wang, R. Peng, Z. Liu Photothermal therapy with immune-adjuvant nanoparticles together with checkpoint blockade for effective cancer immunotherapy Nat. Commun., 7 (2016), Article 13193

14 R.D. Weeratna, S.R. Makinen, M.J. McCluskie, H.L. Davis TLR agonists as vaccine adjuvants: comparison of CpG ODN and Resiquimod (R-848) Vaccine, 23 (45) (2005), pp. 5263-5270

15 K.A. Michaelis, M.A. Norgard, X.X. Zhu, P.R. Levasseur, S. Sivagnanam, S.M. Liudahl, K.G. Burfeind, B. Olson, K.R. Pelz, D.M.A. Ramos, H.C. Maurer, K.P. Olive, L.M. Coussens, T.K. Morgan, D.L. Marks The TLR7/8 agonist R848 remodels tumor and host responses to promote survival in pancreatic cancer (vol 10, 4682, 2019) Nat. Commun., 10 (2019), p. 4682

16 J. Xu, L. Xu, C. Wang, R. Yang, Q. Zhuang, X. Han, Z. Dong, W. Zhu, R. Peng, Z. Liu Near-infrared-triggered photodynamic therapy with multitasking upconversion nanoparticles in combination with checkpoint blockade for immunotherapy of colorectal cancer ACS Nano, 11 (5) (2017), pp. 4463-4474

17 Q. Fan, Z. Chen, C. Wang, Z. Liu Toward biomaterials for enhancing immune checkpoint blockade therapy Adv. Funct. Mater., 28 (37) (2018), Article 1802540

18 X. Han, R. Wang, J. Xu, Q. Chen, C. Liang, J. Chen, J. Zhao, J. Chu, Q. Fan, E. Archibong, L. Jiang, C. Wang, Z. Liu In situ thermal ablation of tumors in combination with nano-adjuvant and immune checkpoint blockade to inhibit cancer metastasis and recurrence Biomaterials, 224 (2019), Article 119490

19 X. Zhang, C. Yi, L. Zhang, X. Zhu, Y. He, H. Lu, Y. Li, Y. Tang, W. Zhao, G. Chen, C. Wang, S. Huang, G. Ouyang, D. Yu Size-optimized nuclear-targeting phototherapy enhances the type I interferon response for "cold" tumor immunotherapy Acta Biomater., 159 (2023), pp. 338-352

20 X. Xue, Y. Huang, R. Bo, B. Jia, H. Wu, Y. Yuan, Z. Wang, Z. Ma, D. Jing, X. Xu, W. Yu, T.-y. Lin, Y. Li Trojan Horse nanotheranostics with dual transformability and multifunctionality for highly effective cancer treatment Nat. Commun., 9 (1) (2018), p. 3653

21 W. Yu, X. Xue, A.-H. Ma, Y. Ruan, H. Zhang, F. Cheng, Y. Li, C.-X. Pan, T.-Y. Lin Self-assembled nanoparticle-mediated chemophototherapy reverses the drug resistance of bladder cancers through dual AKT/ERK inhibition Adv. Ther., 3 (8) (2020), Article 2000032

22 P. Huang, D. Wang, Y. Su, W. Huang, Y. Zhou, D. Cui, X. Zhu, D. Yan Combination of small molecule prodrug and nanodrug delivery: amphiphilic drug–drug conjugate for cancer therapy J. Am. Chem. Soc., 136 (33) (2014), pp. 11748-11756

23 X. Chi, G.M. Peters, F. Hammel, C. Brockman, J.L. Sessler Molecular recognition under interfacial conditions: calix[4]pyrrole-based cross-linkable micelles for ion pair extraction J. Am. Chem. Soc., 139 (27) (2017), pp. 9124-9127

24 X. Xue, Y. Huang, X. Wang, Z. Wang, R.P. Carney, X. Li, Y. Yuan, Y. He, T.-y. Lin, Y. Li Self-indicating, fully active pharmaceutical ingredients nanoparticles (FAPIN) for multimodal imaging guided trimodality cancer therapy Biomaterials, 161 (2018), pp. 203-215

25 S. Sindhwani, A.M. Syed, J. Ngai, B.R. Kingston, L. Maiorino, J. Rothschild, P. MacMillan, Y. Zhang, N.U. Rajesh, T. Hoang, J.L.Y. Wu, S. Wilhelm, A. Zilman, S. Gadde, A. Sulaiman, B. Ouyang, Z. Lin, L. Wang, M. Egeblad, W.C.W. Chan The entry of nanoparticles into solid tumours Nat. Mater., 19 (5) (2020), pp. 566-575

26 E.A. Sykes, J. Chen, G. Zheng, W.C.W. Chan Investigating the impact of nanoparticle size on active and passive tumor targeting efficiency ACS Nano, 8 (6) (2014), pp. 5696-5706

27 Q. Chen, L. Xu, C. Liang, C. Wang, R. Peng, Z. Liu Photothermal therapy with immune-adjuvant nanoparticles together with checkpoint blockade for effective cancer immunotherapy Nat. Commun., 7 (2016), Article 13193

28 Y. Hong, J.W.Y. Lam, B.Z. Tang Aggregation-induced emission Chem. Soc. Rev., 40 (11) (2011), pp. 5361-5388

29 X. Xue, S. Jin, C. Zhang, K. Yang, S. Huo, F. Chen, G. Zou, X.-J. Liang Probe-inspired nano-prodrug with dual-color fluorogenic property reveals spatiotemporal drug release in living cells ACS Nano, 9 (3) (2015), pp. 2729-2739

30 X. Xue, Y. Zhao, L. Dai, X. Zhang, X. Hao, C. Zhang, S. Huo, J. Liu, C. Liu, A. Kumar, W.-Q. Chen, G. Zou, X.-J. Liang Spatiotemporal drug release visualized through a drug delivery system with tunable aggregation-induced emission Adv. Mater., 26 (5) (2014), pp. 712-717

31 S. Reitsma, D.W. Slaaf, H. Vink, M.A.M.J. van Zandvoort, M.G.A. oude Egbrink The endothelial glycocalyx: composition, functions, and visualization Pflüg. Arch. Eur. J. Phy., 454 (3) (2007), pp. 345-359

32 T. Panaretakis, O. Kepp, U. Brockmeier, A. Tesniere, A.C. Bjorklund, D.C. Chapman, M. Durchschlag, N. Joza, G. Pierron, P. van Endert, J. Yuan, L. Zitvogel, F. Madeo, D.B. Williams, G. Kroemer Mechanisms of pre-apoptotic calreticulin exposure in immunogenic cell death EMBO J., 28 (5) (2009), pp. 578-590

33 M. Obeid, A. Tesniere, F. Ghiringhelli, G.M. Fimia, L. Apetoh, J.L. Perfettini, M. Castedo, G. Mignot, T. Panaretakis, N. Casares, D. Metivier, N. Larochette, P. van Endert, F. Ciccosanti, M. Piacentini, L. Zitvogel, G. Kroemer Calreticulin exposure dictates the immunogenicity of cancer cell death Nat. Med., 13 (1) (2007), pp. 54-61

34 Y. Guo, Q. Zhang, Q. Zhu, J. Gao, X. Zhu, H. Yu, Y. Li, C. Zhang Copackaging photosensitizer and PD-L1 siRNA in a nucleic acid nanogel for synergistic cancer photoimmunotherapy Sci. Adv., 8 (16) (2022), Article eabn2941

35 F. Chen, Y. Wang, J. Gao, M. Saeed, T. Li, W. Wang, H. Yu Nanobiomaterial-based vaccination immunotherapy of cancer Biomaterials, 270 (2021), Article 120709

36 R.B. Patel, R. Hernandez, P. Carlson, J. Grudzinski, A.M. Bates, J.C. Jagodinsky, A. Erbe, I.R. Marsh, I. Arthur, E. Aluicio-Sarduy, R.N. Sriramaneni, W.J. Jin, C. Massey, A.L. Rakhmilevich, D. Vail, J.W. Engle, T. Le, K. Kim, B. Bednarz, P.M. Sondel, J. Weichert, Z.S. Morris Low-dose targeted radionuclide therapy renders immunologically cold tumors responsive to immune checkpoint blockade Sci. Transl. Med., 13 (602) (2021) eabb3631

37 C. Twyman-Saint Victor, A.J. Rech, A. Maity, R. Rengan, K.E. Pauken, E. Stelekati, J.L. Benci, B. Xu, H. Dada, P.M. Odorizzi, R.S. Herati, K.D. Mansfield, D. Patsch, R.K. Amaravadi, L.M. Schuchter, H. Ishwaran, R. Mick, D.A. Pryma, X. Xu, M.D. Feldman, T.C. Gangadhar, S.M. Hahn, E.J. Wherry, R.H. Vonderheide, A.J. Minn Radiation and dual checkpoint blockade activate non-redundant immune mechanisms in cancer Nature, 520 (7547) (2015), pp. 373-377

38 C.S. Jin, J.F. Lovell, J. Chen, G. Zheng Ablation of hypoxic tumors with dose-equivalent photothermal, but not photodynamic, therapy using a nanostructured porphyrin assembly ACS Nano, 7 (3) (2013), pp. 2541-2550

39 D.-L. Zhang, L.-W. Qu, L. Ma, Y.-C. Zhou, G.-Z. Wang, X.-C. Zhao, C. Zhang, Y.-F. Zhang, M. Wang, M.-Y.J.C.l. Zhang Genome-wide identification of transcription factors that are critical to non-small cell lung cancer Cancer Lett., 434 (2018), pp. 132-143

Acknowledgements

The financial of this work was supported by the National Natural Science Foundation of China (81803002, 82172084, PI: Xue) and UC Davis faculty startup fund (PI: Li) and Merit Review Award (# 1I01 BX003840, PI: Pan) from the United States (U.S.). Department of Veterans Affairs Biomedical Laboratory Research and Development Program. The contents do not represent the views of the U.S. Department of Veterans Affairs or the United States Government.

Scheme 1. Schematic illustration of the multimodal nanoplatform (PDR NPs) and the anti-cancer activities.

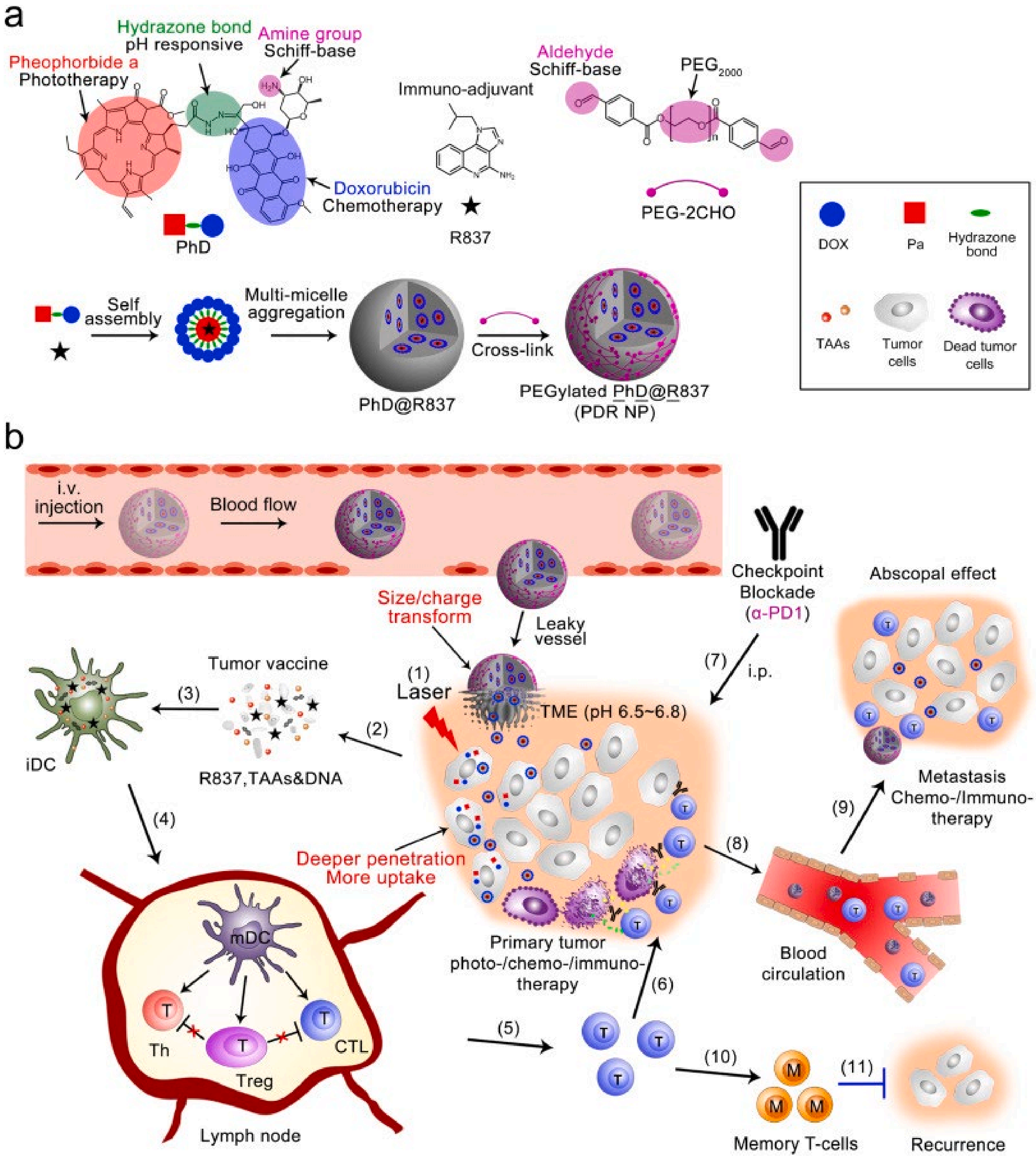

a) The self-assembly of PDR NPs and the corresponding functionality of each component. The amphiphilic PhD monomers first assembled into ultrasmall micelles driven by hydrophobic force, then instantaneously aggregated into larger nanoparticles via multi-micelle aggregation. The gray particle is actually the schematic illustration of multiple micelles. b) The therapeutic process of PDR NPs to primary, distant and recurrence tumor. The process includes: 1) PDR NPs exert a phototherapeutic effect upon the laser treatment; 2) PDR NP-mediated phototherapy ablates the tumor cells, releases TAAs, exposes DNA fragments and free R837; 3) TAAs, DNA and R837 are ingested by immature DC (iDC); 4) DC maturation induced by the stimulation of ICD, STING and TLR pathways. Mature DCs present TAAs to T cells in the lymph node; 5) T cells are primed; 6) the primary tumor cells are treated by the combinatorial therapies of phototherapy, chemotherapy and immunotherapy; 7) immune checkpoint inhibitor (α-PD1) is administered to reactivate T cells; 8) T cells roam in blood circulation; 9) Combination of chemotherapy and immunotherapy treats metastatic tumor; 10) T cells differentiate into memory T cells and 11) prevent tumor recurrence. α-PD1, antibody of programmed cell death protein 1; DNA, deoxyribonucleic acid.

Fig. 1. Characterization of PDR NPs.

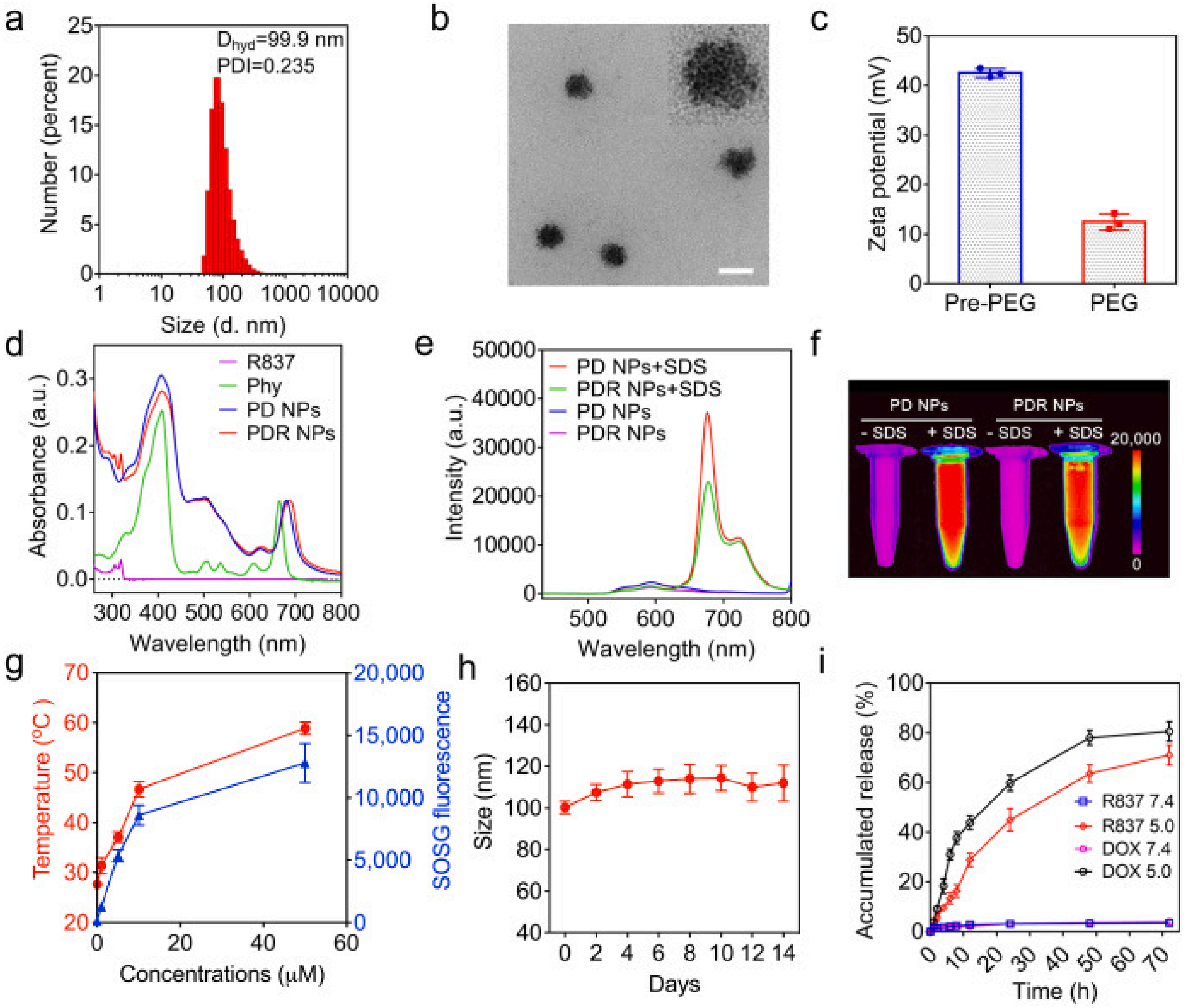

a) The size distribution of PDR NPs measured by dynamic light scattering (DLS). b) Transmission electron microscopic (TEM) micrograph showed the morphology of PDR NPs. The scale bar is 100 nm. c) Surface charge changes of PDR NPs before (Pre-PEG) and after (PEG) the PEGylation. d) UV–vis spectra of R837, Phy (Pa-hydrazide), PD NPs and PDR NPs. e) Fluorescence spectra of PD and PDR NPs with or without the addition of SDS. The excitation is 412 nm. f) NIRF imaging of the samples in e). To measure the optical spectra, the concentrations of Phy, PD NPs and PDR NPs were calculated based on the equivalent molar of 5 µM Phy. g) Photo-induced hyperthermia and reactive oxygen species (ROS) production of PDR NPs. Singlet oxygen sensor green (SOSG) probe was used to indicate ROS. The laser power was set to 0.6 w/cm2 for 3 min. h) Serum stability of PDR NPs indicated by size distribution. 50 µM PDR NPs were incubated with 10% fetal bovine serum and applied to DLS measurement. i) Accumulated drug release of PDR NPs (50 µM). Lysosomal pH (5.0) was employed to cleave the hydrazone bond for the drug releases of DOX and R837.

Fig. 2. In vitro evaluation of PDR NPs.

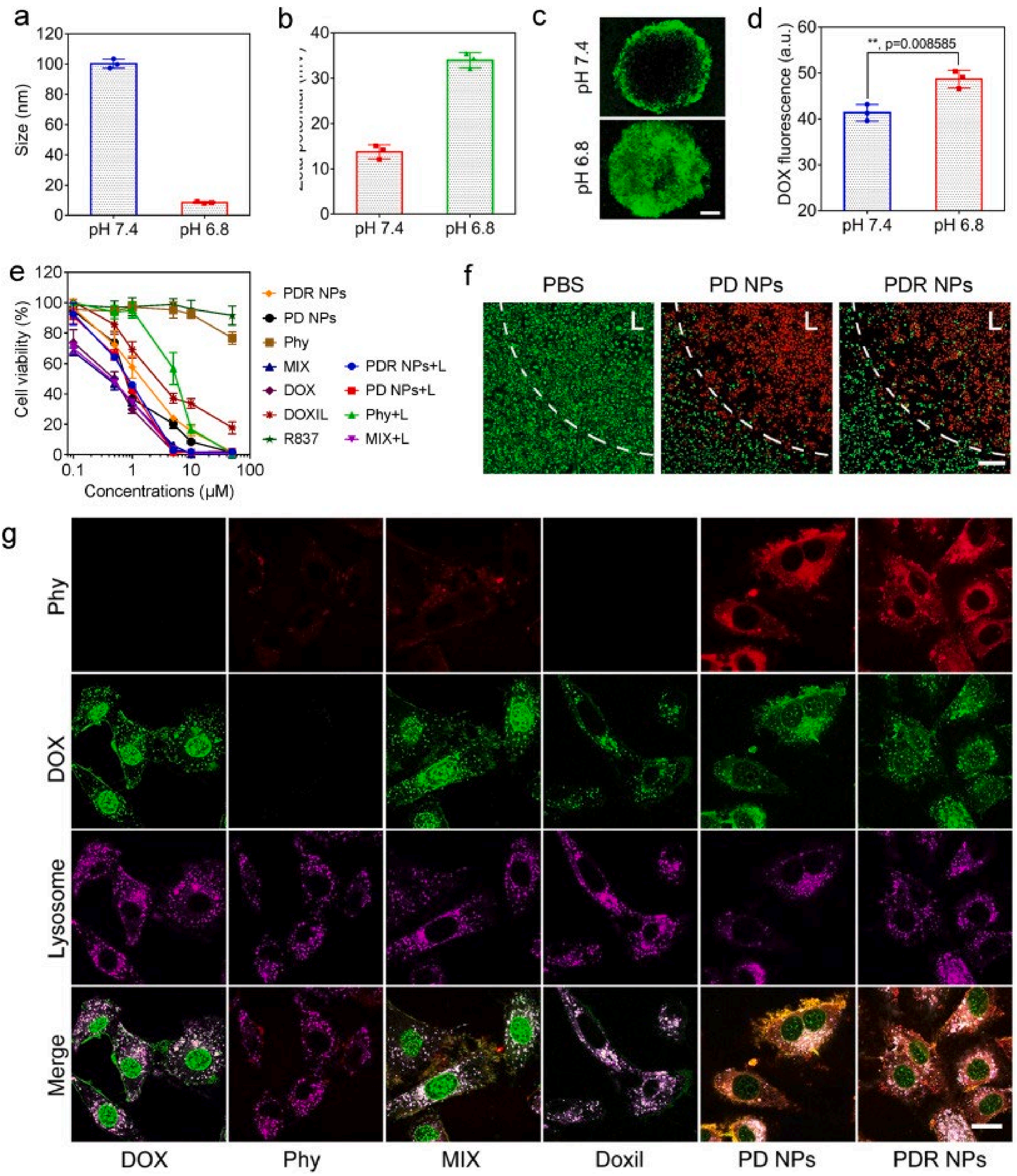

a) Size changes of PDR NPs triggered by pHe (6.5). b) The changes in surface charge of PDR NPs when treated with pH 6.5. The incubation time was set as 12 h to make the PDR NPs undergo the size and charge transformation completely. c) The penetration of PDR NPs in UPPL bladder cancer cell spheroid. Tumor spheroids were incubated with PDR NPs in the cell culture medium with pH of 7.4 and 6.5, respectively. The penetration of PDR NPs was visualized by monitoring the fluorescence of DOX. The images were collected at the same layer of the confocal scanning. The scale bar is 20 μm. d) Strongly positive charge elevated the cellular uptake of PDR NPs. e) Cell viability of PDR NPs and the control groups. The Pa-containing groups were applied to 3 min light treatment, and further incubated for another 12 h. The non-light-treated cells were incubated for another 12 h without any further treatments. The concentrations of different formulations were calculated based on the equivalent molar concentration of Pa or DOX. Phy is Pa with hydrazide residue. f) Controllable phototherapeutic effect of PD NPs and PDR NPs. The scale bar is 200 µm. PBS is phosphate buffer saline. g) Subcellular distribution of DOX, Pa, MIX, Doxil, PD NPs and PDR NPs observed by confocal laser scanning microscopy (CLSM). The scale bar is 20 µm.

Fig. 3. The phototherapy-triggered ICD and DC maturation of PDR NPs.

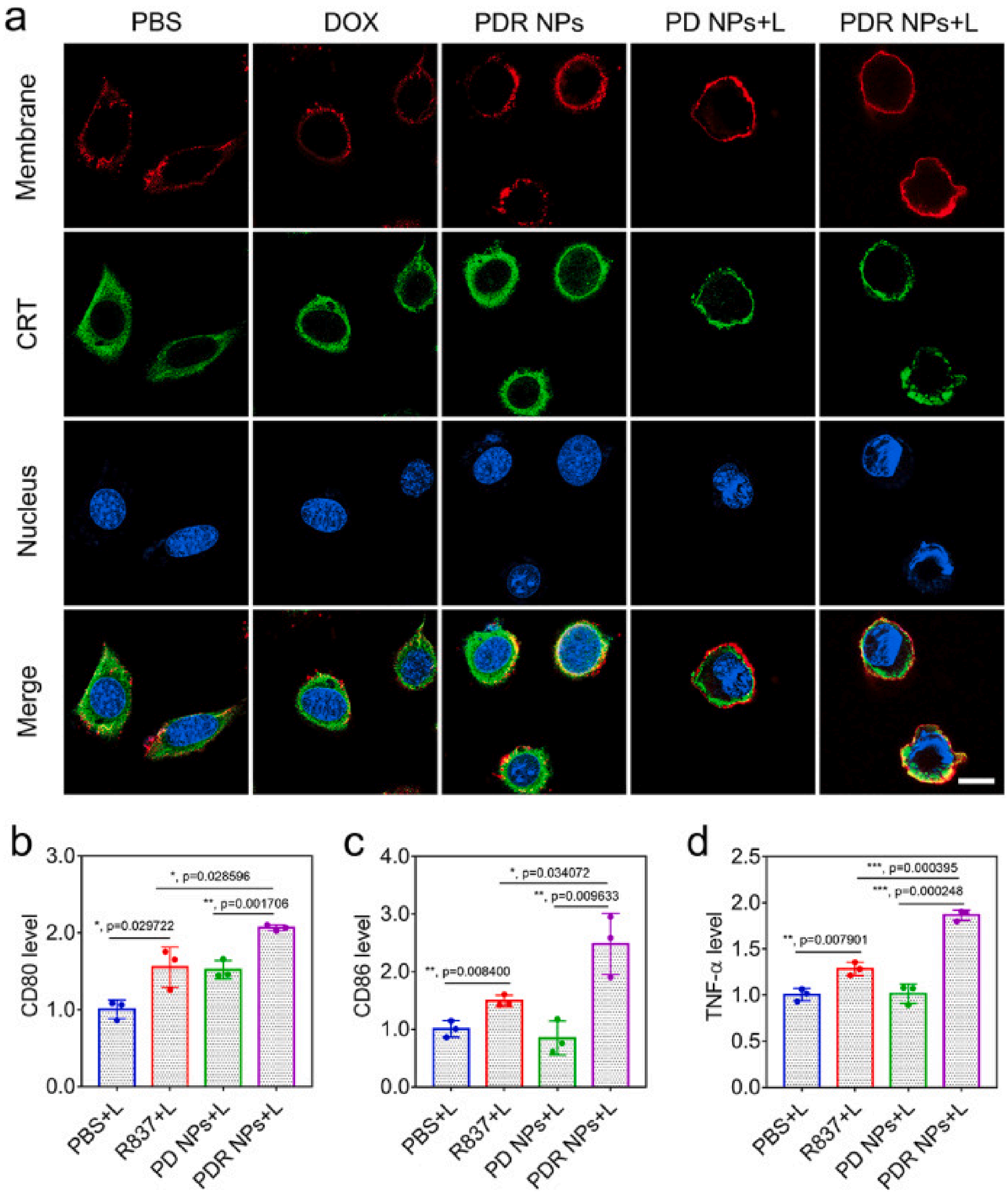

a) Calreticulin (CRT) dislocation of the UPPL cells treated with different materials. The scale bar is 20 μm. qPCR quantification of b) CD80, c) CD86 and level of d) TNF-α expressed on PDR NPs treated DC2.4 mouse DC. Equivalent amounts of PBS, R837 and PD NPs were set as control. For the experiments related to photo-treatment at the cellular level, a laser panel covering a broader range was employed. To differentiate the intense laser in the animal experiments, we use light to instead laser in the cell experiments. "L" denotes light irradiation.

Fig. 4. DC maturation stimulated by multiple aspects.

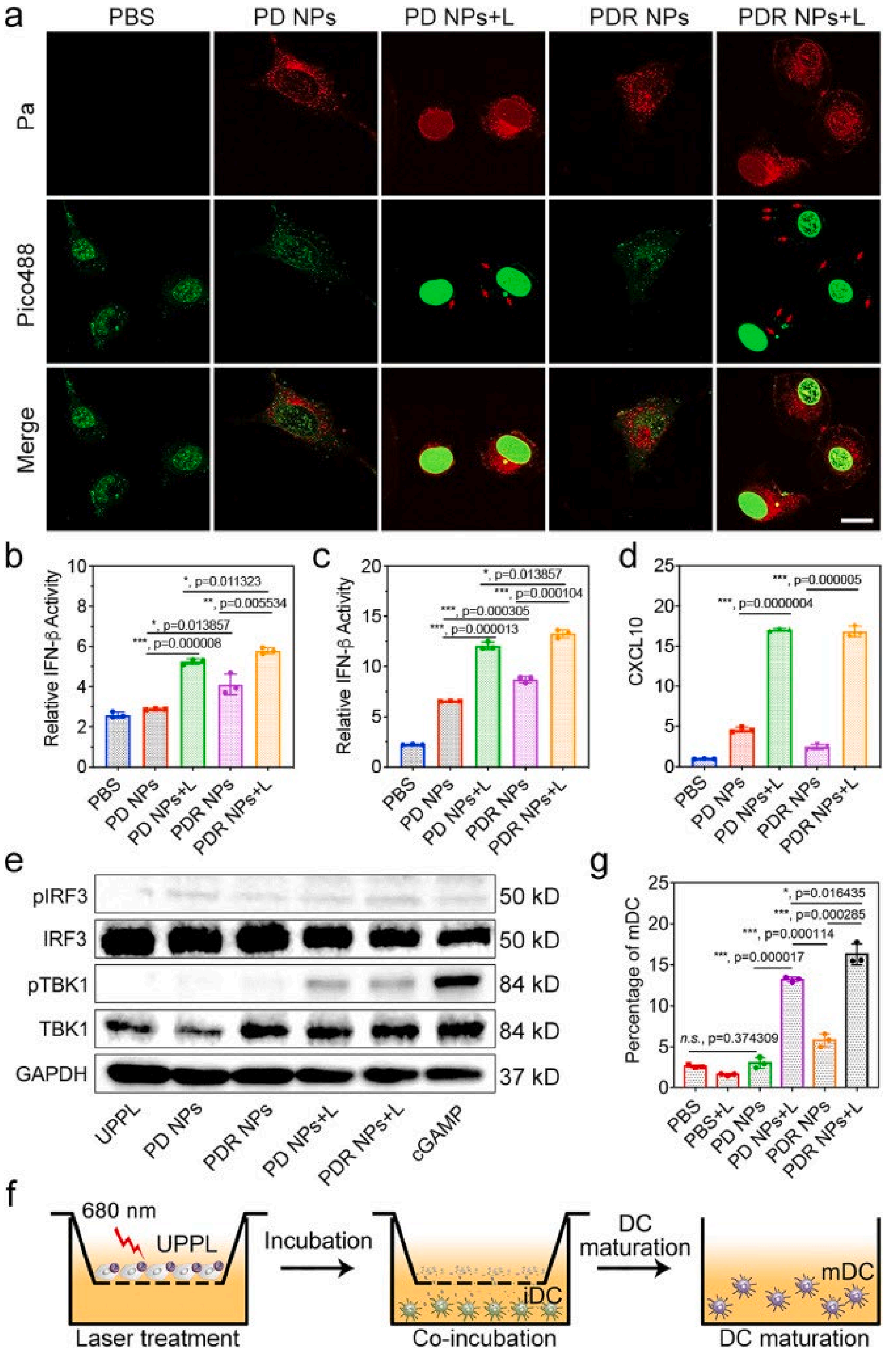

a) CLSM micrographs showed the DNA damage of UPPL cells caused by phototherapy. Red arrows point DNA outside the nucleus. The scale bar is 20 μm. b) 24 h and c) 48 h of IFN-β expressed by THP-1 cell with STING reporter gene. d) CXCL 10 level of THP-1 cells. e) Western blot investigated the phosphorylation of the downstream proteins in the STING pathway. The THP-1 cells were treated by PD NPs and PDR NPs with or without light treatment. The treating dose of cGAMP was 10 μM. f) Schematic illustration of transwell experiment employed to evaluate the DC maturation promoted by the combinatorial effects of ICD, STING and TLR pathway. g) FACS evaluation of mature DC by quantifying the CD86 marker.

Fig. 5. In vivo performance of PDR NPs.

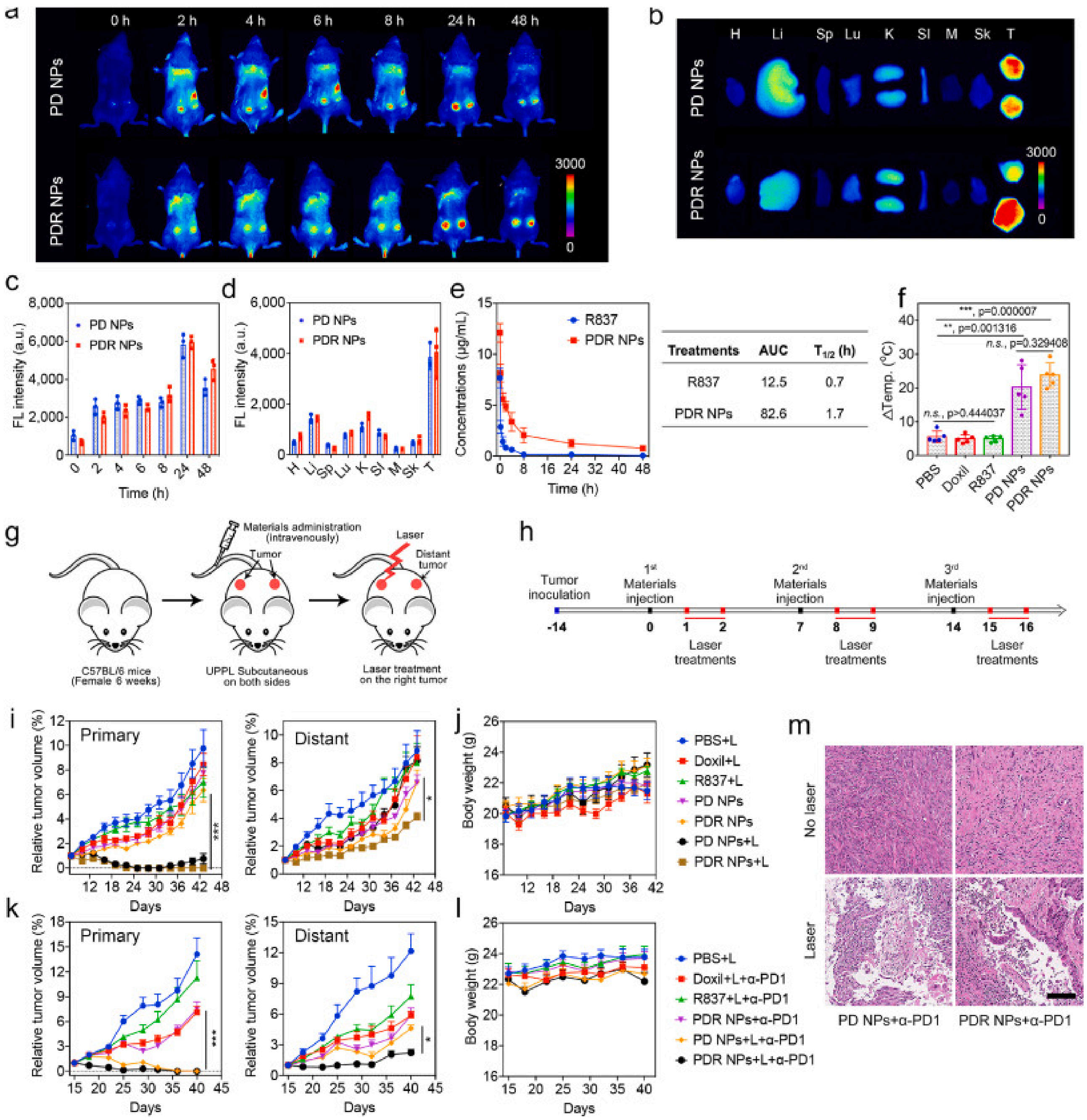

Treatments	AUC	$T_{1/2}$ (h)
R837	12.5	0.7
PDR NPs	82.6	1.7

a) In vivo NIRF imaging of PD and PDR NPs on UPPL bladder tumor-bearing mice. b) Ex vivo NIRF imaging of the organs of PD or PDR NPs treated mice in a). H, heart; Li, liver; Sp, spleen; Lu, lung; K, kidney; SI, small intestine; M, muscle; Sk, skin. T, tumor. Quantification of the c) in vivo fluorescence at tumor site and d) ex vivo imaging of PD NPs and PDR NPs treated mice. e) The pharmacokinetic profile of free R837 and PDR NPs (PD NP@R837). The area under the curve (AUC) and half-life time ($T_{1/2}$) of free R837 and PDR NPs were calculated and listed in the right table. f) Photothermal effect of PDR NPs on UPPL bladder tumor-bearing mice. g) Establishment of the UPPL tumor-bearing mouse model. h) The animal treatment procedures. i) Tumor volumes of the primary and distant tumors along with the treatments (without α-PD1). j) Bodyweight of the mice in the treatment of i). k) Tumor volumes of the primary and distant tumor along with the materials plus α-PD1. l) Body weight of the mice in the treatment of k). The α-PD1 was i.p. injected twice per week for two consecutive weeks. m) H&E stain showed that the laser treatment could destroy the tumor tissue. The scale bar is 100 μm. The dose of PDR NPs was 10 mg/kg (calculated based on PhD monomer). The doses of Doxil, R837, PD NPs were calculated equivalently to PDR NPs.

Fig. 6. The immune response elicited by the nanoplatform.

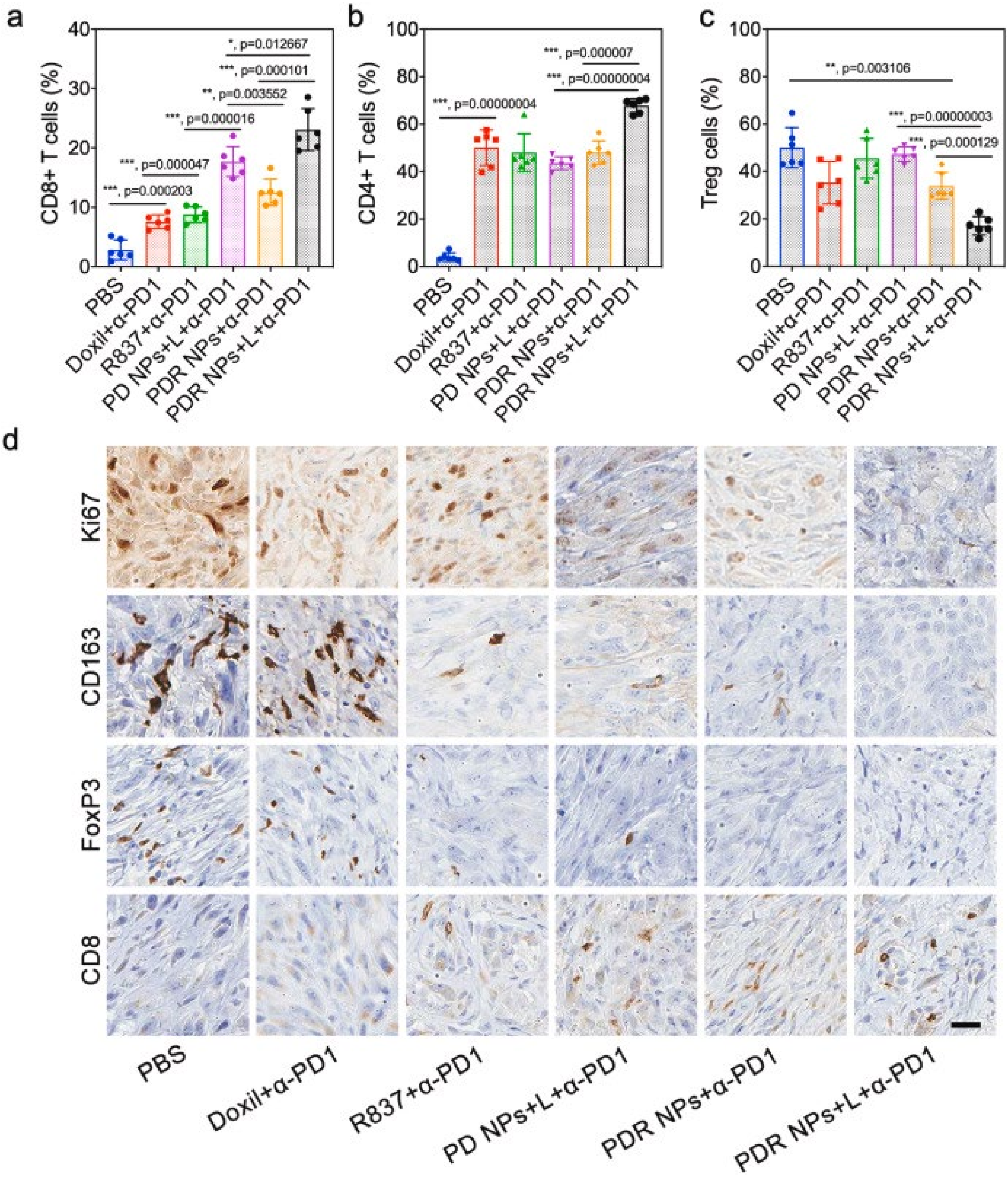

Statistical analysis of the populations of a) $CD4^+$ T cells, b) $CD8^+$ T cells and c) Treg cells, according to the flow cytometry analysis. d) Immunohistopathology analysis of the different biomarkers in the distant tumors received different treatments. ki67 indicated the cell proliferation; CD163 is a biomarker of M2 TAMs; FoxP3 is the marker of Treg cells; CD8 is the marker of cytotoxic T lymphocytes. The scale bar = 20 μm.

Fig. 7. The memory effect of immunotherapy elicited by our nanoplatforms.

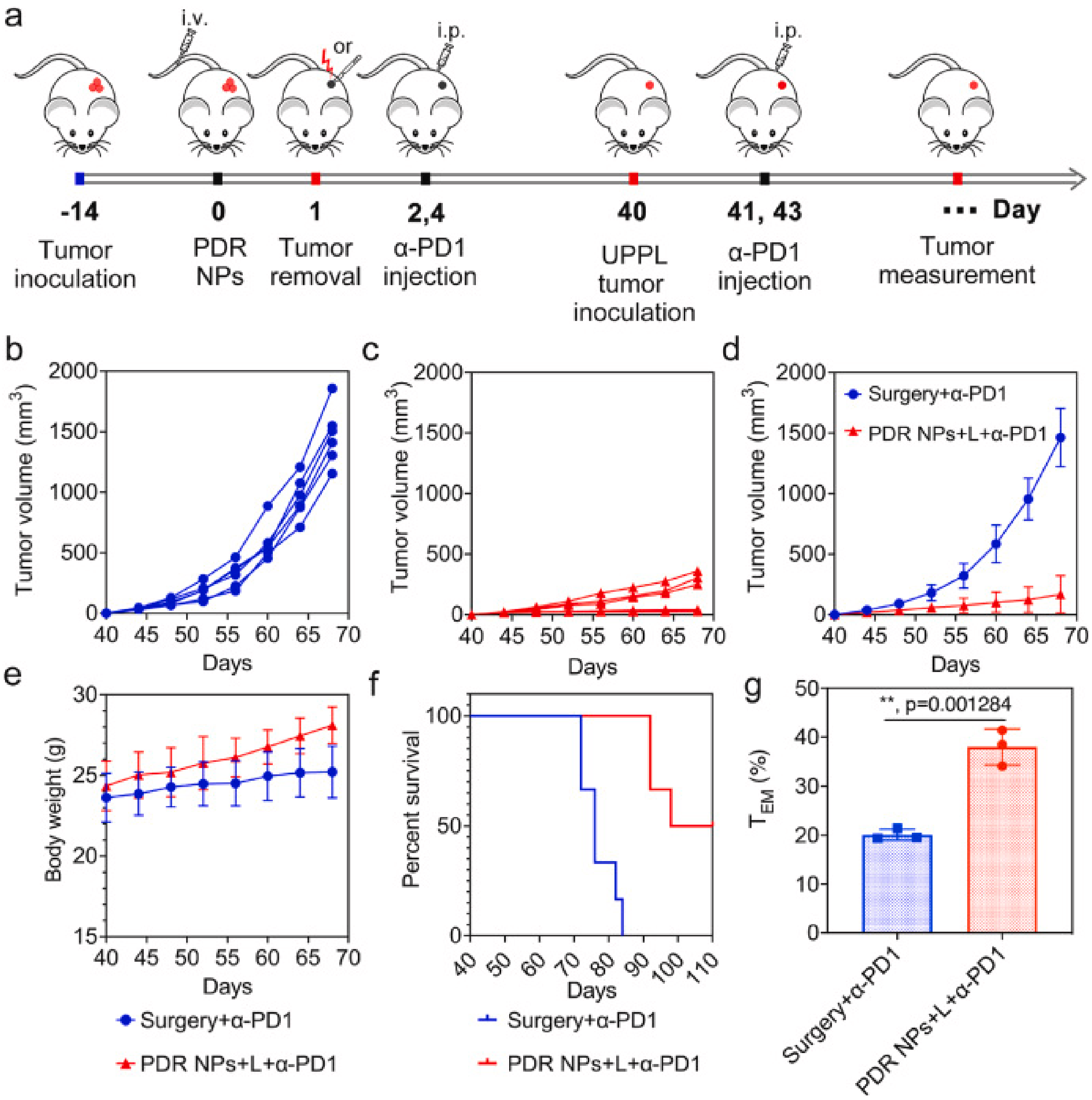

a) Schematic illustration of the tumor-rechallenging experiments. Spaghetti curves of the tumor size changes of the b) surgery-applied mice and c) nanoplatform (PDR NPs) plus laser-treated mice. d) The changes in tumor size of the mice (n = 6) treated by surgery and nanoplatform. e) Body weight changes of the mice. f) Survival curves of the treated mice. g) The effector memory T cells (T_{EM}, $CD3^{+}CD8^{+}CD44^{+}CD62L-$) of different treatments (n = 3).